Novel Resonance-Assisted Electromagnetic-Transport Phenomena

by

André B. Kurs

Submitted to the Department of Physics
in partial fulfillment of the requirements for the degree of

Doctor of Philosophy in Physics

at the

MASSACHUSETTS INSTITUTE OF TECHNOLOGY

February 2011

MASSACHUSETTS INSTITUTE OF TECHNOLOGY
OCT 3 1 2011
LIBRARIES
ARCHIVES

© André B. Kurs, MMXI. All rights reserved.

The author hereby grants to MIT permission to reproduce and distribute publicly paper and electronic copies of this thesis document in whole or in part.

Author .....
Department of Physics
January 20, 2011

Certified by .....
Steven G. Johnson
Associate Professor of Applied Mathematics
Thesis Supervisor

Certified by .....
Marin Soljačić
Associate Professor of Physics
Thesis Supervisor

Accepted by .....
Krishna Rajagopal
Associate Department Head for Education

Novel Resonance-Assisted Electromagnetic-Transport Phenomena

by

André B. Kurs

Submitted to the Department of Physics
on January 20, 2011, in partial fulfillment of the
requirements for the degree of
Doctor of Philosophy in Physics

Abstract

We first demonstrate theoretically and experimentally that electromagnetic resonators with high quality factors (Q) can be used to transfer power efficiently over distances substantially larger than the characteristic dimensions of the resonators by operating in a so-called "strongly coupled" regime. We next generalize the notion of strongly coupled resonances to a system comprising one power source and multiple receivers in a regime of broad practical applicability and show that, by appropriately tuning the parameters of the system, it is possible to significantly improve the overall efficiency of the wireless power transfer relative to the single-source and single-receiver configuration. We experimentally verify the predicted improvement in efficiency for a system consisting of one large source (area $\sim$ 1 m^2) coupling to two much smaller receivers of dimensions comparable to those of many portable electronic devices (area $\sim$ 0.07 m^2). Next, we present a novel design for an electrical conductor whose structure is optimized to have the lowest achievable resistance in the 2–20 MHz frequency range, where it can offer performance an order of magnitude better than the best currently available conductors. The two following chapters deal with energy transport in photonic crystals. We first investigate numerically how a square lattice of dielectric rods may be used to collimate a laser beam and the feasibility of using this system as a chemical sensor. Finally, we present and demonstrate through specific examples a systematic and general procedure, which is both computationally inexpensive and straightforward to implement, for coupling strongly dissimilar waveguides with 100% transmission.

Thesis Supervisor: Steven G. Johnson
Title: Associate Professor of Applied Mathematics

Thesis Supervisor: Marin Soljačić
Title: Associate Professor of Physics

Acknowledgments

It has been a great privilege and a pleasure to learn physics from—and work with—Profs. Steven Johnson and Marin Soljačić, my co-supervisors. I am also grateful to Steven and Marin for their patience and for actively motivating me to complete this work over the past year. I would like to thank Prof. John Joannopoulos and Marin for introducing me to the field of photonics, for allowing me join them in their research on wireless power transfer, and for broadening my horizons by encouraging me to perform experimental as well as theoretical work. I have benefitted from discussions with my collaborators on the work presented here and would like to acknowledge them by name: Marcus Dahlem, Prof. Peter Fisher, Dr. Katie Hall, Prof. Erich Ippen, Dr. Aristeidis Karalis, Dr. Morris Kesler, Prof. Leslie Kolodziejski, Robert Moffatt, Dr. Gale Petrich, Ta-Ming Shih, as well as Steven, Marin, and JJ. I also extend my gratitude to all the members of the JDJ/MS/SGJ group. Some of the theoretical work presented here was conducted on the premises of WiTricity Corporation, and I would like to thank them for their support and for the honor of working with such a talented group of individuals.

Contents

List of Figures

Chapter 1

Overview

A substantial part of this dissertation deals with phenomena arising in systems of coupled electromagnetic modes that are well described by a subset of the powerful phenomenological techniques collectively known as coupled-mode theories [29, 30]. Chapter 2 provides a physically intuitive and heuristic derivation of the coupled-mode theory expressions that will be used throughout much of our work. Chapters 3, 4, and 5 either deal directly with or (in the case of Chapter 5) were originally inspired by the tantalizing possibility of making efficient wireless power transfer feasible for practical applications. The mechanism for power transfer that we consider here relies on the near-field interactions between the electromagnetic fields of different resonators rather than on their radiative far-field, and we show that although near-field interactions, by their very nature, decay faster as a function of distance than radiative fields [36], it is possible, with proper design, to use them to achieve efficient power transfer (where the precise meaning of "efficient" may depend on the requirements of the particular application) when a source (the object transmitting the power) and a device (the object on the receiving end of the transfer) are separated by distances multiple times greater than their characteristic dimensions. Furthermore, this near-field solution does not suffer from many of the drawbacks of a radiative approach such as lack of omnidirectionality (if the radiation is not directed), the need for complicated tracking mechanisms (if it is), necessity of a clear line-of-sight between the source and the device at practical frequency ranges for radiative power transfer,

as well as more stringent safety concerns for radiative systems [35].

Chapter 3 starts by expressing the condition for efficient wireless power transfer between two resonators in the framework of coupled-mode theory. Within this framework, we are able to identify a "strongly coupled" region in the parameter space of the coupled resonators where the efficiency of the transfer is sufficiently high for a wide range of applications. Although the coupled-mode theory treatment is general enough to apply to essentially any system of interacting resonators, we focus on electromagnetic resonances for a concrete demonstration of the principle of strongly coupled resonances. For our first experimental validation of midrange wireless power transfer using near-field coupling, we build helical self-resonant coils which rely on their distributed inductance and capacitance to resonate (in contrast to the lumped inductance and capacitance of a textbook RLC circuit). We develop from first principles an approximate analytical theory for self-resonant coils that matches the experimental results reasonably well for a wide variety of parameters and proves to be quite useful in predicting the expected performance of self-resonant coils before they are built, thus aiding in their design. Finally, we measure the coupled-mode theory parameters for our self-resonant coils and, in a separate experimental setup, the efficiency of the power transfer and find the latter to be in good agreement with the optimal efficiency predicted from the coupled-mode theory parameters. With the self-resonant coils built for this project (measuring 60 cm in diameter) we are able to achieve an efficiency $\simeq$ 50% at a separation of 2 m between the center of the coils.

Chapter 4 generalizes the coupled-mode theory treatment to a system containing one source interacting with an arbitrary number of devices in the limit where the coupling between the source and a device dominates over the coupling of that particular device to any other device. This setup approximates a real-world scenario where a large resonator (e.g., embedded in a wall) serves as the source of power for a multitude of much smaller receivers, which could potentially be integrated into electronic devices. We find that one can achieve significant gains in the overall efficiency of the system by simultaneously powering multiple properly tuned devices, and that this improvement in performance could lead to decent overall efficiencies even if the

source is only marginally strongly coupled to any particular receiver. We demonstrate these results in a laboratory experiment coupling one large source ($\simeq$ 4 times the area of the self-resonant coils in Chapter 2) to two small sources ($\simeq$ 1/16 times the area of the source). We perform this considerably more complicated experiment using a very different methodology from that of the previous chapter and find the directly measured efficiency to be in excellent agreement with the prediction from coupled-mode theory.

In Chapter 5 we present an original design for an electrical conductor—consisting of a number of mutually insulated coaxial conducting shells—that has much lower resistance in the 2–20 MHz range (which is of particular interest to our wireless power transfer approach) than the best currently available conductors: a solid wire or litz wire (litz wire is a braid of many thin and mutually insulated strands [76, 24, 57]). In the course of introducing our new conductor design, we also elucidate the physical effects at work in a conductor at radiofrequencies (such as the skin-depth effect and proximity losses) and analyze why litz wires, which work quite well at frequencies below 1 MHz, become impractical above $\sim$ 2 MHz. One obvious application of our proposed conductor would be to build magnetic resonators for midrange wireless transfer with improved performance and/or more compact design, although our novel design could possibly be of use to any electrical application in this frequency range.

The next two chapters shift the focus away from wireless power transfer and towards applications of photonic crystals. Photonic crystals are man-made periodic dielectric structures whose properties can be tailored to enable an exceptional amount of control over the propagation light and a variety of unique physical effects [37]. In Chapter 6, we show how we used computer simulations to aid in the design of a subsequently fabricated photonic crystal slab composed of silicon rods which supported the propagation of a light beam with nearly no diffraction, a phenomenon known as supercollimation. We also quantitatively compare the expected performance of supercollimation in our rod slab to an alternative photonic crystal consisting of a lattice of holes in a dielectric slab.

Finally, Chapter 7 outlines a general procedure that could be used to couple very

dissimilar waveguides with 100% transmission. This technique is more easily understood in a coupled-mode theory approach and is in principle applicable to any pair of waveguides as long as a few simple conditions (weak-coupling of both waveguides to a resonance and among themselves) are satisfied. The prescription is typically easy to implement and computationally cheap, as we demonstrate explicitly for different combinations of three different photonic crystal waveguides.

Chapter 2

Temporal coupled-mode theory

2.1 Introduction

In this chapter we give an overview of the coupled-mode theory formalism [29] that will be used in much of this thesis. In general, a couple-mode theory may refer to any of a set of abstract approaches used to treat diverse problems such as coupled parallel waveguides [28, 33], tapered waveguides [40, 56], resonant cavities coupled to waveguides [20, 21, 74] and many other physical systems (e.g., see [30] and references therein). A common thread in coupled-mode theory methods is to expand the physical field in a finite basis and extract the coefficients governing the dynamics of the field by enforcing some additional constraint such as conservation of energy [29], time-reversal symmetry [74], Lorentz reciprocity [12], or using a variational principle [31]. Here we focus on two cases of importance to the problems treated in this thesis: a system of discrete coupled resonators relevant to our analysis of midrange wireless power transfer (Chapters 3 and 4) and a resonant cavity weakly coupled to waveguides (Chapter 7). In the first case we will show—following the approach of [29]—that if the system is time-invariant (so that the geometrical and material properties do not vary in time) and the overlaps of the fields due to different resonators are sufficiently small, then the total energy of the system can be expressed to good approximation as the sum of the energies of the individual resonators and the coupling and decay coefficients can be derived in a straightforward way by enforcing energy conservation

and linearity. Similarly, we derive equations describing the evolution of the cavity coupled to waveguides as done in [37] by assuming that the cavity is weakly coupled to each waveguide (and that the direct coupling between waveguides is weaker still and can be ignored to leading order), and enforcing time-invariance, time-reversal invariance, energy conservation and linearity.

2.2 Coupled-mode theory of discrete coupled resonators

For concreteness, we shall focus on electromagnetic resonances in this section, although the same arguments are applicable to other types of resonances (e.g., acoustic and nuclear) as long as they obey the same general physical principles. We start by considering a set of N lossless resonators, and assume that we have found the harmonic solution to Maxwell's equations for each individual resonator m in the absence of all others:

$$\nabla \times \mathbf{e}_m(\mathbf{r}) = i\omega_m \mu_m(\mathbf{r}) \mathbf{h}_m(\mathbf{r}), \tag{2.1}$$

$$\nabla \times \mathbf{h}_m(\mathbf{r}) = -i\omega_m \epsilon_m(\mathbf{r}) \mathbf{e}_m(\mathbf{r}), \tag{2.2}$$

where $\epsilon_m(\mathbf{r})$ and $\mu_m(\mathbf{r})$ are the time-invariant permittivity and permeability profiles associated with resonator m, and ω_m its characteristic frequency. In addition to Eqs. 2.1 and 2.2, $\mathbf{e}_m(\mathbf{r})$ and $\mathbf{h}_m(\mathbf{r})$ must also satisfy the boundary conditions associated with the resonator. For convenience the modes are normalized such that

$$\frac{1}{4} \int d\mathbf{r} \left[\epsilon_m(\mathbf{r}) |\mathbf{e}_m(\mathbf{r})|^2 + \mu_m(\mathbf{r}) |\mathbf{h}_m(\mathbf{r})|^2 \right] = 1. \tag{2.3}$$

Given Eqs. 2.1, 2.2, and 2.3, the time-dependent electric and magnetic fields can be written as $\mathbf{E}_m(\mathbf{r}, t) = a_m(t)\mathbf{e}_m(\mathbf{r})$ and $\mathbf{H}_m(\mathbf{r}, t) = a_m(t)\mathbf{h}_m(\mathbf{r})$, $|a_m(t)|^2$ corresponds to

the energy stored in the resonator, and the time evolution of $a_m(t)$ is governed by

$$\dot{a}_m(t) = -i\omega_m a_m(t). \tag{2.4}$$

We now relax the assumption that the resonators are lossless, and consider the quality factor Q_m of the resonator traditionally defined as [36]

$$Q_m = \omega_m \frac{\text{Energy stored in resonator } m}{\text{Average power loss in } m}. \tag{2.5}$$

As long as $Q_m \gg 1$, the solution to Maxwell's equations including losses is well approximated by the lossless solution, and the average power loss is $P_m(t) \propto |a_m(t)|^2$. Using Eq. 2.5, we find

$$\begin{aligned} P_m(t) &= \frac{\omega_m}{Q_m}|a_m(t)|^2 \\ &\equiv 2\Gamma_m |a_m(t)|^2, \end{aligned} \tag{2.6}$$

where we have defined the decay rate $\Gamma_m = \omega_m/(2Q_m)$. Since $P_m(t) = d|a_m|^2/dt = a_m\dot{a}_m^* + \dot{a}_m a_m^*$, Eq. 2.4 can be suitably modified to account for Eq. 2.6 by adding a term proportional to Γ_m:

$$\dot{a}_m(t) = -\left(i\omega_m + \Gamma_m\right) a_m(t). \tag{2.7}$$

So far we have considered each resonator in isolation; let us now consider the resonators in the presence of one another and approximate the resulting electromagnetic fields as an expansion in the modes of the individual resonators:

$$\mathbf{E}(\mathbf{r},t) \simeq \sum_m a_m(t)\mathbf{e}_m(\mathbf{r}), \quad \mathbf{H}(\mathbf{r},t) \simeq \sum_m a_m(t)\mathbf{h}_m(\mathbf{r}). \tag{2.8}$$

A calculation of the electromagnetic energy contained in the fields of Eqs. 2.8 would generally have to take into account mixed terms of the form $\propto a_m a_n^*$. However, provided that the resonators are sufficiently separated in space so that the overlap

integrals between different modes satisfy

$$\left| \int d\mathbf{r} \left[\epsilon \left(\mathbf{e}_m \cdot \mathbf{e}_n^* + \mathbf{e}_m^* \cdot \mathbf{e}_n \right) + \mu \left(\mathbf{h}_m \cdot \mathbf{h}_n^* + \mathbf{h}_m^* \cdot \mathbf{h}_n \right) \right] \right| \ll 1, \tag{2.9}$$

it is a good approximation [33] to neglect such energy cross-terms and take the total energy of the system to be $U_{\text{total}} = \sum_m |a_m(t)|^2$. (This is the case for the systems considered in this thesis, for which the overlap terms are $< 10^{-2}$.) Since $|a_m(t)|^2$ is the energy stored in resonator m, we may find its coupling to another resonator n (ignoring all other resonators for now) by noting that changes in the energy $|a_m(t)|^2$ must be due to a combination of the loss mechanisms embodied in Γ_m and a net transfer of energy to or from the other resonator. The latter effect is due to interference terms in the real part of the Poynting vector $\mathbf{E} \times \mathbf{H}^*/2$; it follows that

$$\frac{d|a_m|^2}{dt} = -2\Gamma_m |a_m|^2 + i \left(a_m^* \kappa_{mn} a_n - a_m \kappa_{mn}^* a_n^* \right), \tag{2.10}$$

where the constant κ_{mn} can be determined by integrating the aforementioned terms of the Poynting vector between the two resonators, or by some equivalent method. Although κ_{mn} is typically a function of the angular frequency ω, it can be self-consistently approximated by its value at the mean of the resonant frequencies $(\omega_m + \omega_n)/2$ as long as it varies slowly within a frequency range $\sim \omega/Q_m$ or $\sim \omega/Q_n$ of that value. In general, there may be additional loss terms induced by one resonator on another, but these terms are sufficiently small here that they can be ignored for our purposes in this thesis (one such effect is considered in [43], which analyzes the interference between the radiative fields of two resonators). We can derive some key properties of κ_{mn} by considering the rate of total energy loss of the two coupled resonators m and n:

$$\begin{aligned} \frac{d}{dt} \left(|a_m|^2 + |a_n|^2 \right) &= -2\Gamma_m |a_m|^2 - 2\Gamma_n |a_n|^2 \\ &+ i \left(a_m^* \kappa_{mn} a_n - a_m \kappa_{mn}^* a_n^* + a_n^* \kappa_{nm} a_m - a_n \kappa_{nm}^* a_m^* \right). \end{aligned} \tag{2.11}$$

Since we have assumed that all loss mechanisms are incorporated in Γ_m and Γ_n, the

second line of Eq. 2.11 must equal zero. Combining that with the fact that the phases of a_m and a_n in Eq. 2.11 are arbitrary, we find that κ_{mn} and κ_{nm} must be real and equal.

From Eqs. 2.7 and 2.10, we see that the time evolution of the $a_m(t)$ for a system of coupled resonators is given by

$$\dot{a}_m(t) = -\left(i\omega_m + \Gamma_m\right) a_m(t) + \sum_{n \neq m} i\kappa_{mn} a_n(t). \tag{2.12}$$

In order to apply this formalism to the analysis of power transfer between resonators, we need to modify Eq. 2.12 to account for the effect a source exciting the resonator and that of a load extracting power from the resonator. The first effect is accounted for by adding a driving term $F_m(t)$ to the right-hand side of Eq. 2.12, while the load is modeled as an additional factor that increases the decay rate of resonator m from Γ_m to $(1 + x_m)\Gamma_m$, and extracts power $2x_m\Gamma_m|a_m(t)|^2$ from it. Our coupled-mode theory description of a system of coupled discrete resonators then reads

$$\dot{a}_m(t) = -\left[i\omega_m + (1 + x_m)\Gamma_m\right] a_m(t) + \sum_{n \neq m} i\kappa_{mn} a_n(t) + F_m(t), \tag{2.13}$$

which provides the starting point for the analyses in Chapters 3 and 4.

2.3 Coupled-mode theory of a resonant cavity coupled to waveguides

We now consider a lossless system comprising a resonant cavity—of resonant frequency ω_0—coupled to N waveguides [37]; Fig. 2-1 is a schematic representation of the case $N = 2$ relevant to Chapter 7. Although we assume the system is lossless in the sense that there is no dissipation in materials or power radiated outside of the structure, the energy contained in the cavity mode can still escape through the waveguides. If the coupling of the cavity to each waveguide is sufficiently weak, the cavity mode is well approximated by the lossless case and, as in Section 2.2, we may define

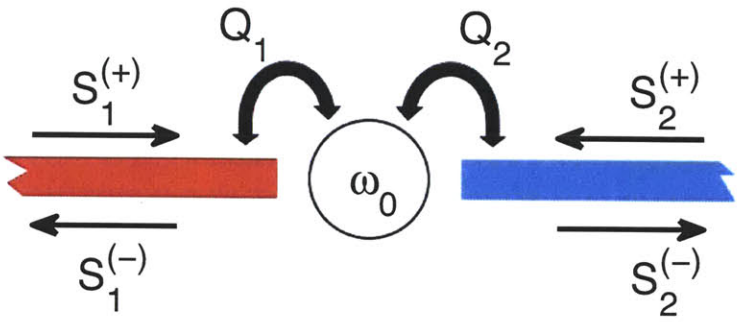

Figure 2-1: Graphical representation of a coupled-mode theory treatment of two waveguides (red and blue strips) coupled by means of a cavity tuned to resonate at the angular frequency ω_0 and couple to each waveguide with quality factors Q_1 and Q_2.

a complex variable $a(t)$ such that $|a(t)|^2$ represents the energy in the cavity. Each waveguide is in turn represented by two complex variables $S_m^{(+)}(t)$ and $S_m^{(-)}(t)$ defined so that the amplitudes squared of their Fourier transforms $\tilde{S}_m^{(+)}(\omega)$ and $\tilde{S}_m^{(-)}(\omega)$ represent the power per unit frequency at ω carried by the waveguide mode traveling towards and away from the cavity, respectively. We further assume that the direct coupling between waveguides can be neglected relative to the coupling between the waveguides and the cavity.

The mode in the cavity can either decay into the outgoing waveguide modes with decay rates $\Gamma_m = \omega_0/(2Q_m)$ [the Q_m being independent from each other as we neglect direct interactions between waveguides to this order of approximation] or be excited by the incoming waveguide modes $S_m^{(+)}(t)$. Since the system is time-invariant and linear, this process is described by an equation of the form

$$\dot{a}(t) = -i\omega_0 \left(1 - i\sum_m \frac{1}{2Q_m}\right) a(t) + \sum_m \alpha_m S_m^{(+)}(t), \tag{2.14}$$

where the parameters α_m represent the coupling between the cavity and the incoming mode. Much like the κ_{mn} in Section 2.2, the α_m are approximated as constants over

the frequency range of interest. Similarly, the power in an outgoing waveguide mode $S_m^{(-)}(t)$ can come from either the decay of the cavity mode or the reflection of its corresponding incoming mode:

$$S_m^{(-)}(t) = \beta_m S_m^{(+)}(t) + \gamma_m a(t), \tag{2.15}$$

where the β_m and γ_m are constants similar to α_m, all of which can be related to ω_0 and Q_m by enforcing conservation of energy and time-reversal invariance. First, consider the decay of the cavity mode to an outgoing waveguide mode m when there is no incoming power. Since the power lost by the cavity must equal the outgoing power, we find from Eqs. 2.14 and 2.15 that

$$-\frac{d|a(t)|^2}{dt} = \frac{\omega_0}{Q_m}|a(t)|^2 = |\gamma_m|^2|a(t)|^2 = \left|S_m^{(-)}(t)\right|^2. \tag{2.16}$$

The relative phase between $a(t)$ and $S_m^{(-)}(t)$ has been undetermined so far, and we may fix it by choosing $\gamma_m = \sqrt{\omega_0/Q_m}$. Let us now run this solution backwards in time (which we are allowed to due to time-reversal symmetry); the incoming mode is now $S_m^{(+)}(t) = \sqrt{\omega_0/Q_m}a(t)$, while the power in the outgoing mode is zero. Combined with Eq. 2.15 this implies that $\beta_m = -1$. Finally, since the energy in the cavity is growing exponentially at a rate $\omega_0|a(t)|^2/Q_m$, we find from Eq. 2.14 and the above value of $S_m^{(+)}(t)$ that $\alpha_m = \sqrt{\omega_0/Q_m}$. The final coupled-mode theory equations then read

$$\dot{a}(t) = -i\omega_0\left(1 - i\sum_m \frac{1}{2Q_m}\right)a(t) + \sum_m \sqrt{\frac{\omega_0}{Q_m}}S_m^{(+)}(t), \tag{2.17}$$

$$S_m^{(-)}(t) = -S_m^{(+)}(t) + \sqrt{\frac{\omega_0}{Q_m}}a(t). \tag{2.18}$$

Thus we see that, for a fixed ω_0, this physical setup can be tuned by varying the various Q_m, a property we exploit in Chapter 7. Let us now apply Eqs. 2.17 and 2.18 to the case of a cavity coupled to two waveguides (Fig. 2-1). We are interested in particular in the transmission $T(\omega) = \left|\tilde{S}_2^{(-)}(\omega)/\tilde{S}_1^{(+)}(\omega)\right|^2$, the fraction of power

coming in from the first waveguide that makes it to the second waveguide when only the first waveguide is excited (here we work in the frequency domain for convenience). Since we have set $\tilde{S}_2^{(+)}(\omega) = 0$, Eq. 2.18 for the second waveguide immediately gives

$$\tilde{S}_2^{(-)}(\omega) = \sqrt{\frac{\omega_0}{Q_2}}\tilde{a}(\omega). \tag{2.19}$$

Meanwhile, Eq. 2.17 becomes

$$-i\omega\tilde{a}(\omega) = -i\omega_0\tilde{a}(\omega) - \left(\frac{1}{2Q_1} + \frac{1}{2Q_2}\right)\omega_0\tilde{a}(\omega) + \sqrt{\frac{\omega_0}{Q_1}}\tilde{S}_1^{(+)}(\omega), \tag{2.20}$$

which combined with Eq. 2.19 gives

$$\tilde{S}_2^{(-)}(\omega) = \frac{\omega_0/\sqrt{Q_1Q_2}}{i(\omega_0 - \omega) + \left(\frac{1}{2Q_1} + \frac{1}{2Q_2}\right)\omega_0}\tilde{S}_1^{(+)}(\omega), \tag{2.21}$$

whence we can read off the transmission

$$T(\omega) = \frac{\omega_0^2/(Q_1Q_2)}{(\omega_0 - \omega)^2 + \left(\frac{1}{2Q_1} + \frac{1}{2Q_2}\right)^2\omega_0^2}. \tag{2.22}$$

When $Q_1 = Q_2$, $T(\omega_0) = 1$ (there is 100% transmission from one waveguide to the other at the resonant frequency of the cavity), a property known as Q-matching [20] that will be used in Chapter 7.

Chapter 3

Wireless power transfer via strongly coupled magnetic resonances

3.1 Summary

We show, using the coupled-mode theory formalism, that a system of two coupled resonances can in principle be operated in a "strongly coupled" regime wherein they transfer power from one another with reasonably high efficiency. We then demonstrate experimentally that a system of two helical self-resonant coils (which resonate due their distributed, as opposed to lumped, inductance and capacitance) fulfills the strong coupling criterion and therefore transfers power efficiently even though the separation between the centers of the coils is many times larger than their characteristic dimensions (i.e., "midrange" distances). We experimentally measure the coupled-mode theory parameters of the coils as well as the efficiency of the coil-to-coil transfer while powering a 60 W light bulb, and find that the measured efficiency agrees well with the optimal efficiency predicted by the coupled-mode theory parameters. Using this setup, we can fully light up the light bulb when the centers of the coils are more than 2 m apart with $\simeq 50\%$ efficiency. We also derive from first prin-

ciples an approximate analytical model for the coils that can predict most quantities of interest within $\sim$ 5%.

3.2 Introduction

Attempts to deliver power wirelessly date from at least the turn of the twentieth century, when Nikola Tesla attempted to develop a scheme to transfer power wirelessly over distance [77]. In the mid-twentieth century, much effort was also devoted to developing a long-range wireless power transfer scheme using radio waves [10]. Over the past decade or so, there has been a proliferation of portable electronic devices (laptops, cell phones, robots, PDAs, etc.) which need to be recharged on a daily basis. As a consequence, interest in wireless power has reemerged [23, 19, 32, 42]. Radiative transfer [78], although perfectly suitable for transferring information, poses a number of difficulties for power transfer applications in that the efficiency of power transfer is very low if the radiation is omnidirectional, and unidirectional radiation requires an uninterrupted line of sight and sophisticated tracking mechanisms. A theoretical paper [44] recently presented a detailed analysis of the feasibility of using resonant objects coupled through the tails of their non-radiative fields for midrange energy transfer. Intuitively, two resonant objects of the same resonant frequency tend to exchange energy efficiently, while dissipating relatively little energy in extraneous off-resonant objects. In systems of coupled resonances (e.g., acoustic, electromagnetic, magnetic, nuclear), there is often a general"strongly coupled"regime of operation [2]. If one can operate in that regime in a given system, the energy transfer is expected to be very efficient. Midrange power transfer implemented in this way can be nearly omnidirectional and efficient, irrespective of the geometry of the surrounding space, with low interference and losses into environmental objects [44]. The above considerations apply irrespective of the physical nature of the resonances. In this dissertation, however, we focus on one particular physical embodiment: magnetic resonances. Magnetic resonances are particularly suitable for everyday applications because most non-metallic and non-magnetic materials do not interact strongly with

magnetic fields, so interactions with environmental objects are minimized. We were able to identify the strongly coupled regime in the system of two coupled magnetic resonances by exploring non-radiative (near-field) magnetic resonant induction at $\sim$ MHz frequencies.

3.3 Coupled-mode theory derivation of the optimal efficiency

Efficient midrange power transfer occurs in particular regions of the parameter space describing resonant objects strongly coupled to one another. Coupled-mode theory is a particularly convenient tool for analyzing systems whose physical properties (e.g., their loss and interaction mechanisms) can be linearized around their resonant frequency. As argued in Section 2.2, a coupled-mode theory description of a set of N resonators reads

$$\dot{a}_m(t) = -\left[i\omega_m + (1+x_m)\Gamma_m\right] a_m(t) + \sum_{n\neq m} i\kappa_{mn} a_n(t) + F_m(t), \tag{3.1}$$

where the indices denote the different resonant objects. The variables $a_m(t)$ are defined so that the energy contained in object m is $|a_m(t)|^2$, ω_m is the resonant angular frequency of that isolated object, Γ_m is its intrinsic decay rate (e.g., due to absorption and radiated losses), and x_m is a normalized external loading through which power can be extracted from the resonator. (Although we omit the specific loading mechanism for generality for now, x_m may be caused by e.g., a loading circuit such as a simple resistor.) The $F_m(t)$ are driving terms and the κ_{mn} are coupling coefficients between the resonant objects indicated by the subscripts.

In this chapter, we limit the treatment to the case of two objects, denoted by source and device, such that the source (identified by the subscript 1) is driven externally at a constant frequency, and the two objects have a coupling coefficient κ. Work is extracted from the device (subscript 2) by means of a loading mechanism that contributes the additional term x_2 to Eq. 3.1. The work extracted is determined by

the power dissipated in the load, that is, $2x_2\Gamma_2|a_2(t)|^2$. Finding the efficiency η of the transfer with respect to the loading involves solving Eq. 3.1 for a 2×2 system with $\kappa_{1,2} \equiv \kappa$, $x_1 = 0$, $F_1 \neq 0$, and $F_2 = 0$. One finds that the efficiency is highest when the source and the device are resonant ($\omega = \omega_1 = \omega_2$), in which case the efficiency as a function of x_2 and $\kappa/\sqrt{\Gamma_1\Gamma_2}$ becomes

$$\begin{aligned} \eta &= \frac{x_2\Gamma_2|a_2|^2}{\Gamma_1|a_1|^2 + (1+x_2)\Gamma_2|a_2|^2} \\ &= \frac{[x_2/(1+x_2)^2][\kappa^2/(\Gamma_1\Gamma_2)]}{1 + [1/(1+x_2)][\kappa^2/(\Gamma_1\Gamma_2)]} \end{aligned} \tag{3.2}$$

Thus we see that the efficiency depends only on the the dimensionless quantity $\kappa/\sqrt{\Gamma_1\Gamma_2}$ (which depends on intrinsic properties of the resonators as well on their coupling) and on the loading factor x_2 which can in principle be tuned to any value we wish. We find that the efficiency is maximized when $x_2 = \sqrt{1+\kappa^2/(\Gamma_1\Gamma_2)}$ and a plot of the optimal efficiency as a function of $\kappa/\sqrt{\Gamma_1\Gamma_2}$ is shown in Fig. 3-1, from which it is apparent that the efficiency of energy transfer is sufficiently high for many applications requiring considerable amounts of power when $\kappa^2/(\Gamma_1\Gamma_2) \gtrsim 1$. This is commonly referred to as the strong coupling regime and can be intuitively understood by noting that κ represents the rate at which energy is exchanged between the resonators, while $\sqrt{\Gamma_1\Gamma_2}$ is a measure of how fast the resonators dissipate energy. If the energy can be whisked away from the source resonator to the device resonator and then to a load which converts that energy into useful work faster than the energy is wasted ($\kappa \gtrsim \sqrt{\Gamma_1\Gamma_2}$), we would expect the overall energy transfer to be reasonably efficient. Resonance plays an essential role in this power transfer mechanism, as the efficiency is improved by approximately ω^2/Γ_2^2 ($\sim 10^6$ for typical parameters) relative to the case of coupled nonresonant objects.

3.4 Theoretical model for self-resonant coils

After some experimentation in the laboratory, we decided to use self-resonant coils for our demonstration of wireless power transfer. Relative to capacitively loaded

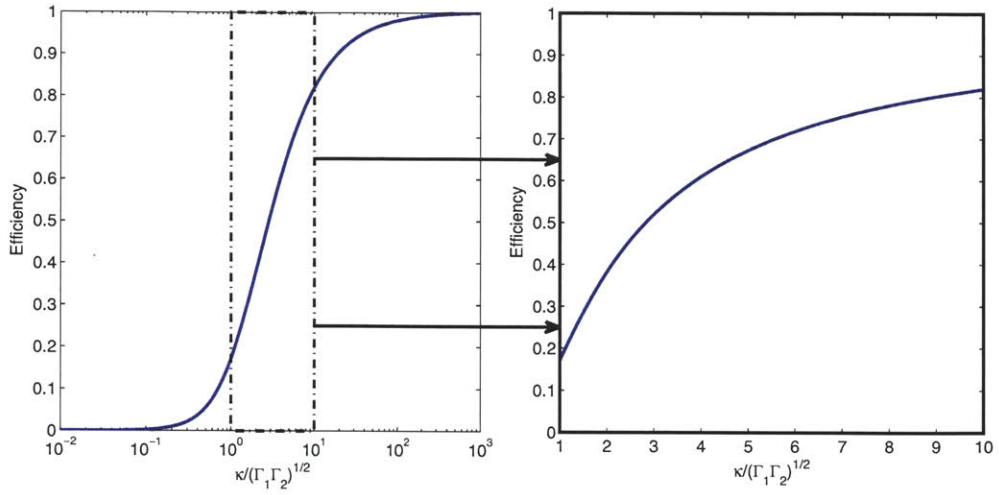

Figure 3-1: Optimal efficiency as a function of the strong-coupling parameter $\kappa/\sqrt{\Gamma_1\Gamma_2}$. Notice how most of the upswing in efficiency occurs within one decade of $\kappa/\sqrt{\Gamma_1\Gamma_2}$. We define the strongly-coupled regime as the parameter space defined by $\kappa/\sqrt{\Gamma_1\Gamma_2} \gtrsim 1$, where the efficiency is sufficiently high for a wide variety of real-world applications.

coils [44]—which were the main alternative—self-resonant coils proved to be easy to build with relatively good reproducibility, had sufficiently low losses for our needs, and did not require very low loss capacitors that could handle high amounts of power. For simplicity, both coils were designed to be identical. Self-resonant coils rely on the interplay between distributed inductance and distributed capacitance to achieve resonance. The coils are made of an electrically conducting wire of total length l and cross-sectional radius a wound into a helix of n turns, radius r, and height h. To the best of our knowledge, there is no exact solution for a finite helix in the literature, and even in the case of infinitely long coils, the solutions rely on assumptions that are inadequate for our system [71]. We have found, however, that a simple quasi-static model is in good agreement (within $\sim$ 5%) with experiment. We start our derivation of our theoretical model by observing that the current must be zero at the ends of the coil, and make the educated guess that the resonant modes of the coil are well approximated by sinusoidal current profiles along the length of the conducting wire. We are interested in the lowest mode, so if we denote by s the parametrization

coordinate along the length of the conductor, such that it runs from $-l/2$ to $+l/2$, then the time-dependent current profile has the form $I_0 \cos(\pi s/l) \exp(i\omega t)$. It follows from the continuity equation for charge that the linear charge density profile is of the form $\lambda_0 \sin(\pi s/l) \exp(i\omega t)$, so that one-half of the coil (when sliced perpendicularly to its axis) contains an oscillating total charge ($q_0 = \lambda_0 l/\pi$) that is equal in magnitude but opposite in sign to the charge in the other half. As the coil is resonant, the current and charge density profiles are $\pi/2$ out of phase from each other, meaning that the real part of one is maximum when the real part of the other is zero. Equivalently, the energy contained in the coil is at certain points in time completely due to the current, and at other points it is completely due to the charge. Using standard techniques from electromagnetism [36], we can define an effective inductance L and an effective capacitance C for each coil as follows:

$$L = \frac{\mu_0}{4\pi |I_0|^2} \int\int d\mathbf{r} d\mathbf{r}' \frac{\mathbf{J}(\mathbf{r}) \cdot \mathbf{J}(\mathbf{r}')}{|\mathbf{r} - \mathbf{r}'|} \tag{3.3}$$

$$\frac{1}{C} = \frac{1}{4\pi\epsilon_0 |q_0|^2} \int\int d\mathbf{r} d\mathbf{r}' \frac{\rho(\mathbf{r})\rho(\mathbf{r})'}{|\mathbf{r} - \mathbf{r}'|} \tag{3.4}$$

where μ_0 is the magnetic constant, ϵ_0 is the electric constant, and the spatial current $\mathbf{J}(\mathbf{r})$ and charge density $\rho(\mathbf{r})$ are obtained respectively from the current and charge densities along the isolated coil in conjunction with a parametrization of the geometry of the object. The integrals in Eqs. 3.3 and 3.4 can then be evaluated by numerical integration (which takes of the order of a second in MATLAB). As defined, L and C have the property that the energy U contained in the coil is given by

$$\begin{aligned} U &= \frac{1}{2} L |I_0|^2 \\ &= \frac{1}{2C} |q_0|^2. \end{aligned} \tag{3.5}$$

Given this relation and the equation of continuity $\partial\rho/\partial t + \nabla \cdot \mathbf{J} = 0$, we find that the resonant frequency must be $f_0 = 1/[2\pi\sqrt{LC}]$. We can now treat this coil as a standard oscillator in coupled-mode theory by defining $a(t) = \sqrt{L/2} I_0(t)$. We can estimate the rate of power dissipation and the Q by noting that the sinusoidal profile

of the current distribution implies that the spatial average of the peak current squared is $|I_0|^2/2$. For a coil with n turns and made of a material with conductivity σ, we modify the standard formulas for the ohmic (R_{ohm}) and radiation (R_{rad}) resistances accordingly:

$$R_{\text{ohm}} = \sqrt{\frac{\mu_0\omega}{2\sigma}}\frac{l}{4\pi a} \tag{3.6}$$

$$R_{\text{rad}} = \sqrt{\frac{\mu_0}{\epsilon_0}}\left[\frac{\pi}{12}n^2\left(\frac{\omega r}{c}\right)^4 + \frac{2}{3\pi^3}\left(\frac{\omega h}{c}\right)^2\right]. \tag{3.7}$$

The first term in Eq. 3.7 is a magnetic dipole radiation term (assuming $r \ll 2\pi c/\omega$, where c is the speed of light); the second term is due to the electric dipole of the coil and is significantly smaller than the first term for our experimental parameters. The coupled-mode theory decay constant for the coil is therefore $\Gamma = (R_{\text{ohm}} + R_{\text{rad}})/(2L)$, and its quality factor is $Q = \omega/(2\Gamma)$. Finally, we find the coupling coefficient $\kappa_{2,1}$ by looking at the work done by the source coil on the the device coil, assuming a steady-state solution in which currents and charge densities have a harmonic time dependence $e^{-i\omega t}$:

$$\begin{aligned} W_{2,1} &= \int d\mathbf{r}\mathbf{E_1}(\mathbf{r})\cdot\mathbf{J}_2^*(\mathbf{r}) \\ &= -\frac{1}{4\pi}\int\int d\mathbf{r}d\mathbf{r}'\left[\mu_0\frac{\mathbf{J_1}(\mathbf{r}')}{|\mathbf{r}-\mathbf{r}'|} + \frac{\rho_1(\mathbf{r}')}{\epsilon_0}\frac{\mathbf{r}'-\mathbf{r}}{|\mathbf{r}-\mathbf{r}'|^3}\right]\cdot\mathbf{J}_2^*(\mathbf{r}') \\ &\equiv -i\omega M I_1 I_2^*, \end{aligned} \tag{3.8}$$

where M is the effective mutual inductance and the subscript 1 indicates that the electric field is due to the source. Upon comparing Eqs. 2.11 and 3.8, one finds that $\kappa \equiv \kappa_{2,1} = \omega M/(2\sqrt{L_1 L_2})$. When the distance D between the centers of the coils is much larger than their characteristic size, κ scales with the D^{-3} dependence characteristic of dipole-dipole coupling. Both κ and Γ are functions of the frequency, and κ/Γ and the efficiency are maximized for a particular value of f, which is usually in the range 1 to 50 MHz for typical geometrical parameters of interest [44]. Thus, picking an appropriate resonant frequency for a given coil size plays a major role in

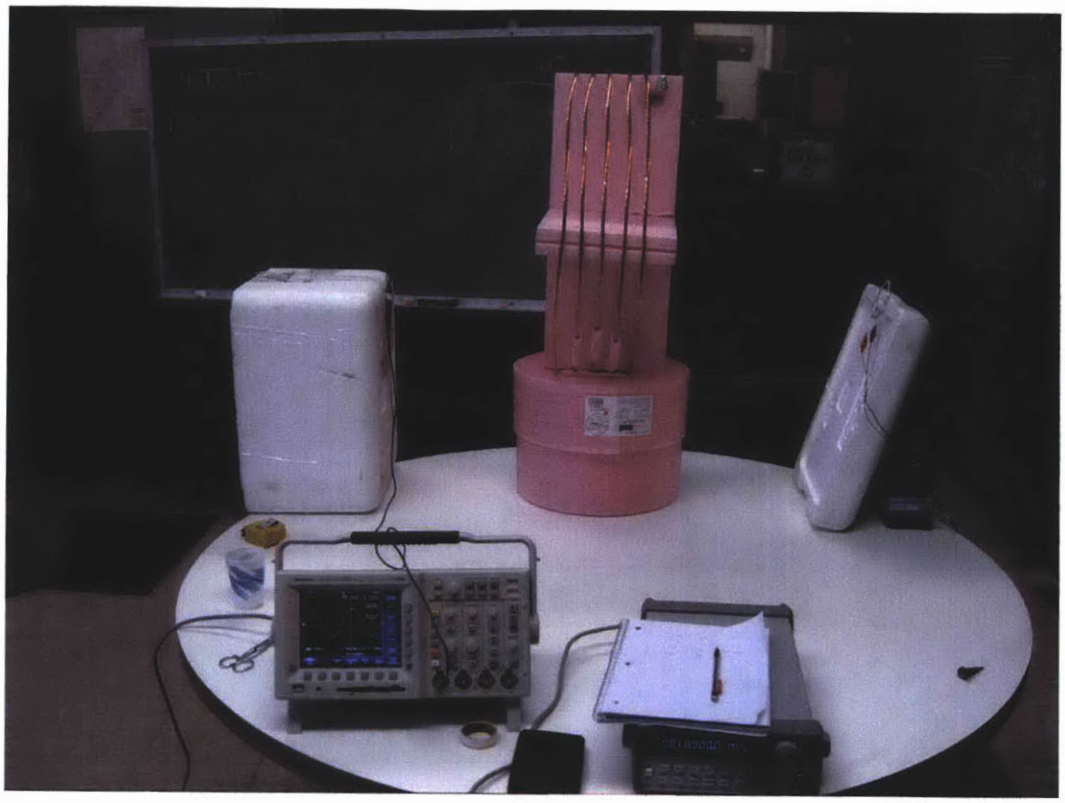

Figure 3-2: Experimental setup for measuring the resonant frequency and quality factor Q of a resonator. The self-resonant coil (center) is excited by a coil connected to a CW source (right), and the amplitude of its excitation is picked up by coil connected to an oscilloscope (left). The quality factor is found from the FWHM of the measured amplitude as the frequency of the CW source is swept.

optimizing the power transfer.

3.5 Experimental measurement of coupled-mode theory parameters and comparison to theory

The parameters for the two identical helical coils built for the experimental validation of the power transfer scheme are $h = 20$ cm, $a = 3$ mm, $r = 30$ cm, and $n = 5.25$. Both coils are made of copper. The spacing between loops of the helix is not uniform, and we encapsulate the uncertainty about their geometry by attributing a 10% ($\pm$ 2 cm) uncertainty to h in the calculations of our analytical model. The

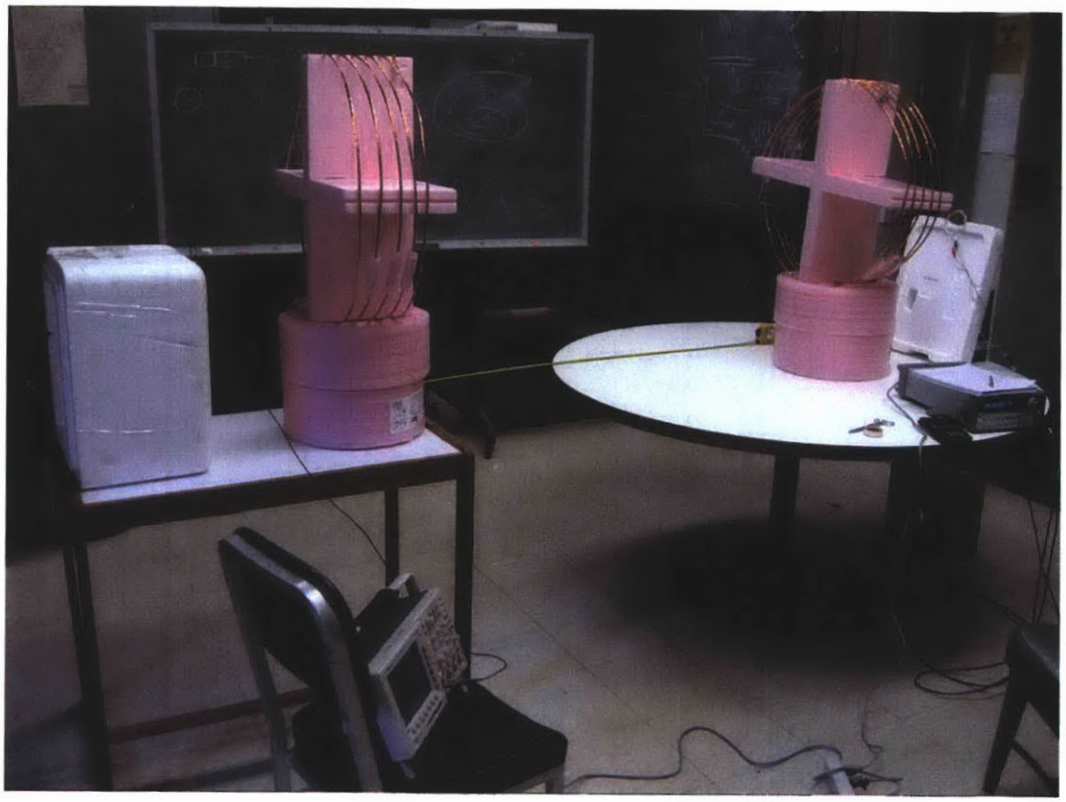

Figure 3-3: Experimental setup for measuring the coupling constant κ. The self-resonant coil on the right is excited by a CW source by means of a small excitation coil, while a pickup coil connected to an oscilloscope measures the amplitude of the excitation of the self-resonant coil on the left. The coupling constant is related to the frequency splitting between the two peaks of the amplitude detected by the oscilloscope as a function of the frequency of the excitation.

expected resonant frequency given these dimensions is $f_0 = 10.56 \pm 0.3$ MHz (the range of values corresponds to the aforementioned uncertainty in the dimensions) and the predicted Q for the loops is estimated to be ~ 2500 (taking $\sigma = 5.9 \times 10^7$ S/m for the copper conductor). The resonant frequency and quality factor of each coil are measured using the setup shown in Fig. 3-2: a CW source excites the self-resonant coil while a pickup coil measures the amplitude of the excitation. Recasting this setup in terms of coupled-mode theory variables involves solving Eq. 3.1 for the case of one driven resonator (denoted by the index 0). The amplitude-squared of the excitation

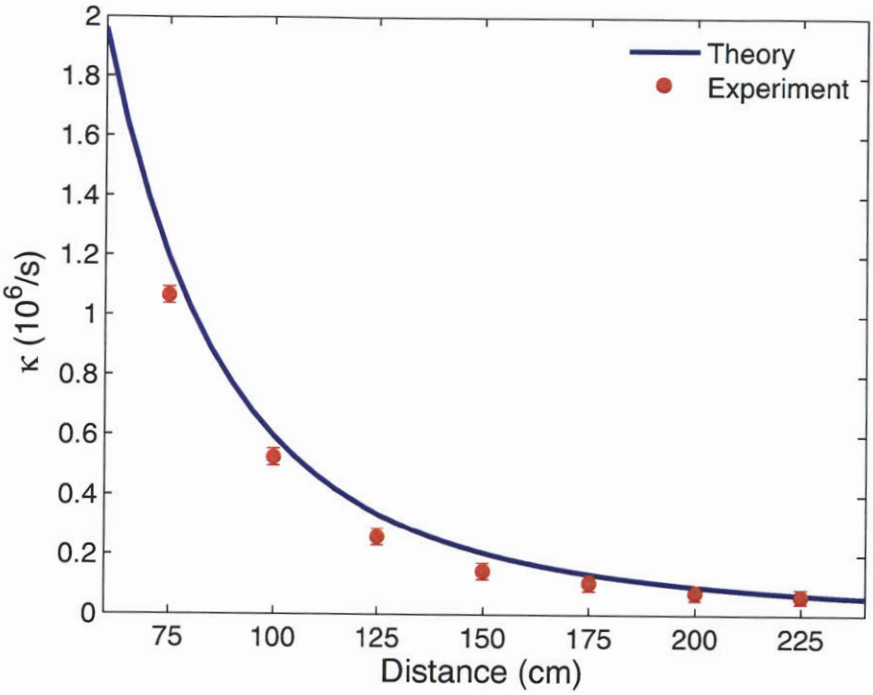

Figure 3-4: Comparison of experimental and theoretical values for κ as a function of the separation between coaxially aligned source and device coils (the wireless power transfer distance).

is readily found to be

$$|a_0|^2 = \frac{|F_0|^2}{(\omega - \omega_0)^2 + \Gamma_0^2}, \tag{3.9}$$

meaning that the resonant frequency corresponds to the frequency at which the amplitude detected by the oscilloscope is maximum and that the Q can be related to the full width at half maximum (FWHM) of the amplitude-squared. We find experimentally that our coils resonate at a frequency of 9.90 MHz, corresponding to an approximately 5% discrepancy with the prediction of our quantitative model, with a Q of 950 $\pm$ 50. We estimate that the more significant difference between measured and predicted values for the Q may be due to our model of resistive losses not taking into account the proximity losses induced by one turn onto the other turns of a coil. We henceforth use the experimentally observed Q and $\Gamma_1 = \Gamma_2 = \Gamma = \omega/(2Q)$ derived from it in all computations.

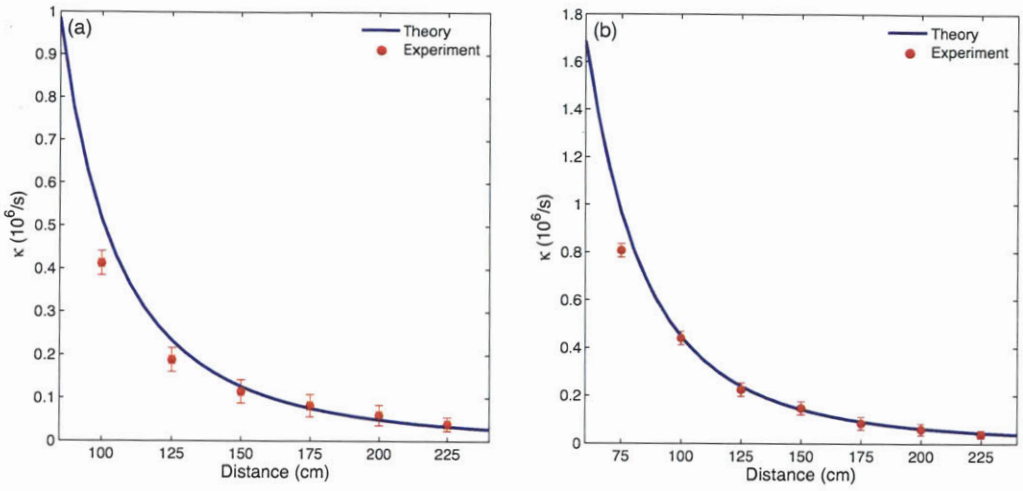

Figure 3-5: Coupling κ vs distance when: (a) the coils are coplanar (b) one of the coils is tilted by 45° away from the coaxial orientation.

We measure the coupling coefficient κ by placing the two self-resonant coils a center-to-center distance D apart, exciting one coil with a CW source and measuring the amplitude of the excitation of the second coil (Fig. 3-3). In coupled-mode theory, this corresponds to a two-resonator system with $F_1 = Fe^{-i\omega t}$, $F_2 = 0$, and $x_1 = x_2 = 0$. The resulting amplitudes are

$$a_1 = \frac{[\Gamma_2 - i(\omega - \omega_2)]\, Fe^{-i\omega t}}{(\omega - \omega_1)(\omega - \omega_2) - i\left[\Gamma_1(\omega - \omega_1) + \Gamma_2(\omega - \omega_2)\right] + \Gamma_1\Gamma_2 + \kappa^2} \tag{3.10}$$

$$a_2 = \frac{-i\kappa Fe^{-i\omega t}}{(\omega - \omega_1)(\omega - \omega_2) - i\left[\Gamma_1(\omega - \omega_1) + \Gamma_2(\omega - \omega_2)\right] + \Gamma_1\Gamma_2 + \kappa^2}. \tag{3.11}$$

Eq. 3.11 implies that when the two resonators are tuned to the same frequency and have the same quality factor ($\omega_1 = \omega_2$ and $\Gamma_1 = \Gamma_2$), the frequency splitting between the two peaks of $|a_2|^2$ is given by $2\sqrt{\kappa^2 - \Gamma^2}$. In this work, we focus on the case where the two coils are aligned coaxially (Fig. 3-4), and although we measured κ as as function of distance for two alternative orientations (Fig. 3-5), we did not proceed with direct measurements of the efficiency for those.

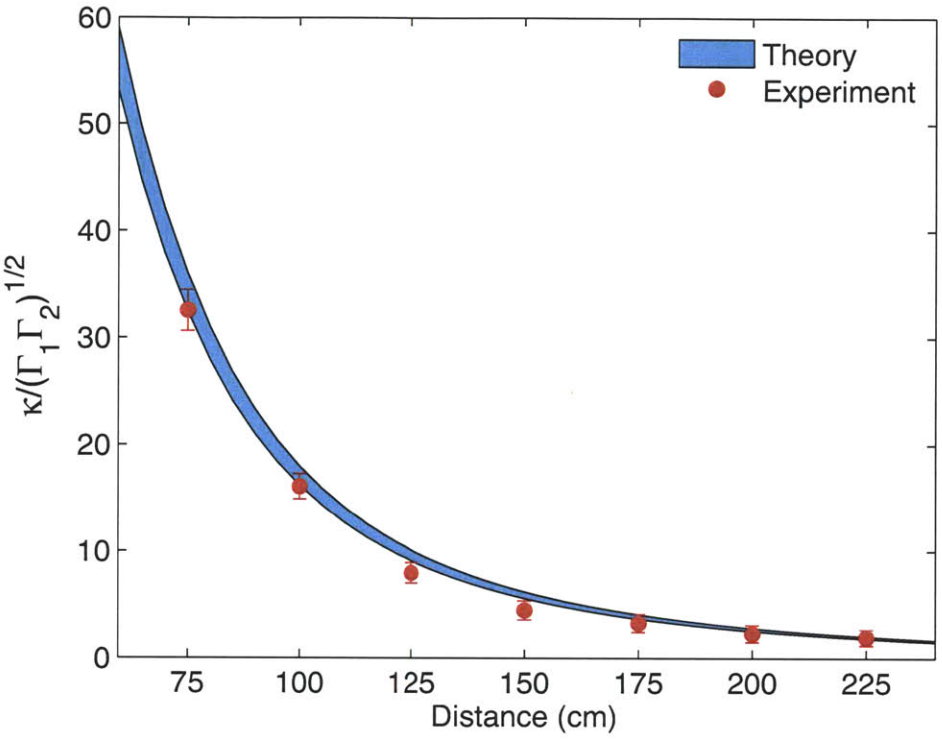

Figure 3-6: Comparison of experimental and theoretical values for the parameter κ/Γ as a function of the wireless power transfer distance. The theory values are obtained by using the theoretical κ and the experimentally measured Γ. The shaded area represents the spread in the theoretical κ/Γ due to the $\simeq 5\%$ uncertainty in Q.

3.6 Measurement of the efficiency

Combining the measured Q with the measured and computed κ, we can plot the strong-coupling parameter $\kappa/\sqrt{\Gamma_1\Gamma_2} = \kappa/\Gamma$ as a function of distance (Fig. 3-6). Comparing the results with Fig. 3-1, we find that we are in the strongly coupled regime throughout the entire range of distances probed.

As our driving circuit, we use a standard Colpitts oscillator [17] whose inductive element consists of a single loop of copper wire 25 cm in radius (Fig. 3-7); this loop of wire couples inductively to the source coil and drives the entire wireless power transfer apparatus. The load consists of a light bulb and is attached to its own loop of insulated wire, which is placed in proximity of the device coil and inductively

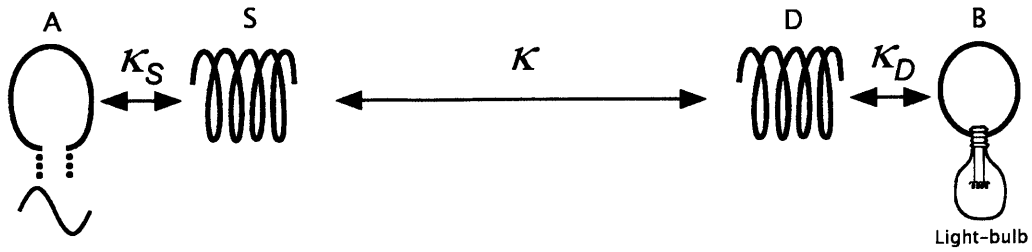

Figure 3-7: Schematic of the experimental setup. A is a single copper loop of radius 25 cm that is part of the driving circuit, which outputs a sine wave with frequency 9.9 MHz. S and D are respectively the source and device coils referred to in the text. B is a loop of wire attached to the load (light bulb). The various κ's represent direct couplings between the objects indicated by the arrows. The angle between coil D and the loop A is adjusted to ensure that their direct coupling is zero. Coils S and D are aligned coaxially. The direct couplings between B and A and between B and S are negligible.

coupled to it. By varying the distance between the light bulb and the device coil, we are able to adjust the parameter x_2 so that it matches its optimal value, given theoretically by $\sqrt{1+(\kappa/\Gamma)^2}$. [The loop connected to the light bulb adds a small imaginary component to $(1+x_2)\Gamma_2$, which shifts the frequency of the device coil but can compensated for by slightly retuning the coil.] We measure the work extracted by adjusting the power going into the Colpitts oscillator until the light bulb at the load glows at its full nominal brightness. We determine the efficiency of the transfer taking place between the source coil and the load by measuring the current at the midpoint of each of the self-resonant coils with a current probe (which does not lower the Q of the coils noticeably). This gives a measurement of the current parameters I_1 and I_2 used in our theoretical model. We then compute the power dissipated in each coil from $P_{1,2} = \Gamma L|I_{1,2}|^2$, and obtain the efficiency from $\eta = P_W/(P_1 + P_2 + P_W)$, where P_W is the power delivered to the load. To ensure that the experimental setup is accurately described by a two-object coupled-mode theory model, we position the device coil such that its direct coupling to the copper loop attached to the Colpitts oscillator is zero. The experimental results are shown in Fig. 3-8, along with the theoretical prediction for maximum efficiency, given by Eq. 3.2. We were able to transfer several tens of watts with the use of this setup, fully lighting up a 60 W

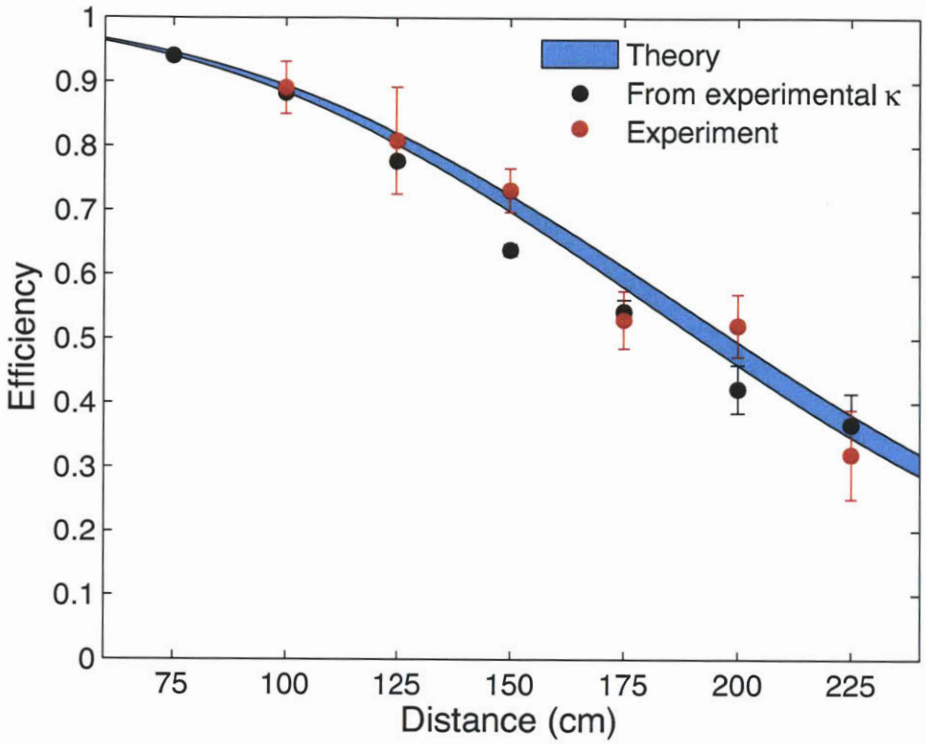

Figure 3-8: Comparison of experimental and theoretical efficiencies as functions of the wireless power transfer distance. The shaded area represents the theoretical prediction for maximum efficiency and is obtained by inserting the theoretical values from Fig. 3-6 into Eq. 3.2, with $x_2 = \sqrt{1+\kappa^2/\Gamma^2}$. The black data points are the maximum efficiency obtained from Eq. 3.2 and the experimental values of κ/Γ from Fig. 3-6. The red dots present the directly measured efficiency, as described in the text.

light bulb from distances more than 2 m away (Fig. 3-9). As a cross-check, we also measured the total power going from the wall power outlet into the driving circuit. The efficiency of the wireless transfer itself is hard to estimate in this way, however, as the efficiency of the Colpitts oscillator itself is not precisely known, although it is expected to be far from 100% [17]. Nevertheless, the ratio of power extracted to power entering the driving circuit gives a lower bound on the efficiency. When transferring 60 W to the load over a distance of 2 m, for example, the power flowing into the driving circuit is 400 W. This yields an overall wall-to-load efficiency of 15%, which is reasonable given the expected efficiency of approximately 50% for the wireless power transfer at that distance and the low efficiency of the Colpitts oscillator.

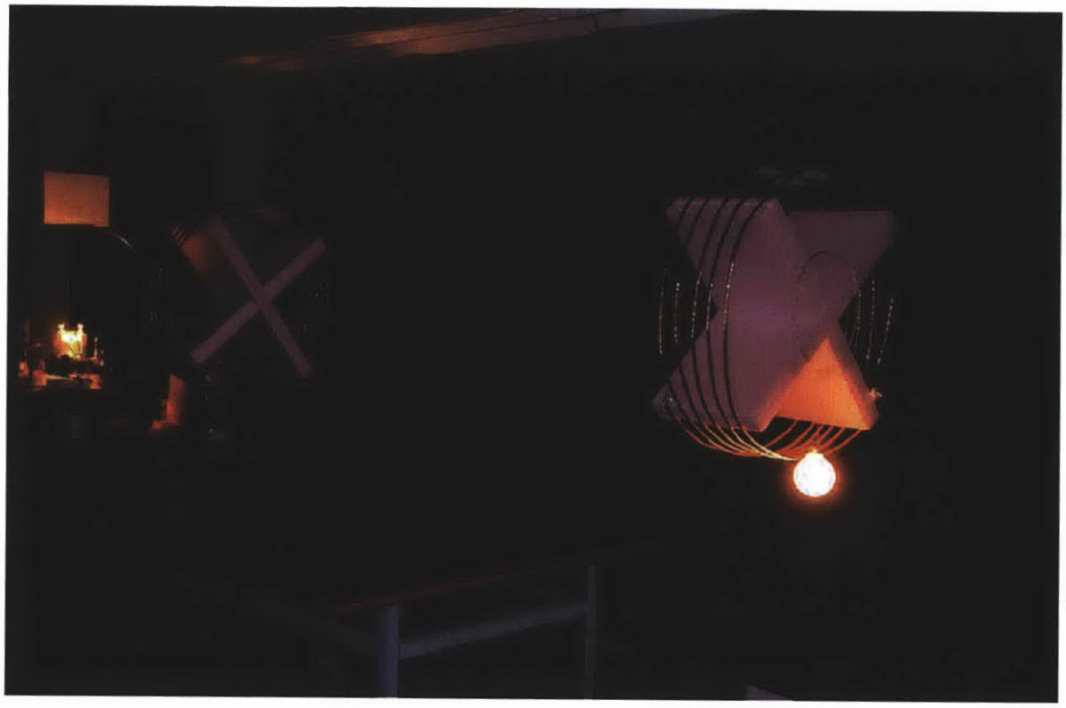

Figure 3-9: Photograph of the laboratory setup showing all of the key elements illustrated in Fig. 3-7. The self-resonant coils are suspended by pieces of insulated string attached to the ceiling. (Image credit: Aristeidis Karalis)

3.7 Conclusion and outlook

Although the two coils are currently of identical dimensions, it is principle possible to make the device coil small enough to fit into portable devices while maintaining the general performance shown here. It should also be possible to considerably improve the wall-to-load efficiency by driving the setup with a high-efficiency RF amplifier. Both of these issues will be addressed in the next chapter.

Chapter 4

Midrange power transfer to multiple devices

4.1 Summary

This chapter takes the basic concept of using self-resonant coils to effect midrange wireless power transfer explored in the previous chapter and expands upon it in a number of significant ways. For the case of a dilute system of device resonators (where the direct coupling between the source and each device dominates over the direct coupling between the devices), we provide exact expressions for the maximum efficiency attainable and for the optimal matching condition, and quantify the improvement in efficiency that can be obtained by powering multiple devices simultaneously. We experimentally validate the possibility of using a large source resonator to power one or more smaller resonators, an important step towards a potential real-world application of the technology of midrange wireless power transfer: a larger resonator embedded in a wall or a piece of furniture powering multiple small resonators embedded in portable electronic devices. We have also employed an improved experimental methodology which allows for in situ measurements of all the relevant coupled-mode theory parameters as well as for direct measurements of the efficiency.

4.2 Overview

Although our first demonstration of efficient midrange wireless power transfer [48] (Chap. 3) used identical resonators for convenience, the method of using high-Q electromagnetic resonators—or a high-Q resonator of any kind [44]—can easily be extended to asymmetrical designs for the source and device. Indeed, other research groups applied the same principles to scenarios that featured a high degree of asymmetry between source and device [70, 11]. These investigations are relevant to potential applications which require the devices to be small enough to be integrated (preferably seamlessly) into portable devices, yet the constraints on the size of the source may be less stringent. One could imagine, for example, a relatively large source embedded in a wall or a piece of furniture powering a multitude of compact devices.

We can obtain a quick estimate of how the dimensionless coupling coefficient $k = 2\kappa/\omega$ of the system scales with the relative sizes of and the distances between the resonators involved by noting that, if the interaction between the coils is predominantly magnetic and the the coils are separated by a center-to-center distance D substantially larger than their characteristic dimensions, then the leading contribution to k will come from the dipole-dipole interaction of the coils, which scales as D^{-3} [36]. Additionally, because of Faraday's law, and assuming that the magnetic field generated by the first coil is approximately uniform over the dimensions of the second coil, the electromotive force induced around the second coil is proportional to its area (and vice versa). The simplest dimensionless quantity that we can form out of the areas of two coils (denoted by A_1 and A_2) and their center-to-center distance which has the requisite properties, namely reciprocity, D^{-3} dependence, and $k \to 0$ if either $A_1 \to 0$ or $A_2 \to 0$ is $(A_1 A_2)^{3/4}/D^3$, so we conclude that the leading-order dependence of the coupling on the geometry of the setup at midrange distances is

$$k \propto \frac{(A_1 A_2)^{3/4}}{D^3}. \tag{4.1}$$

Thus we see that if we keep the product of the areas of the coils constant, the coupling between them should stay roughly constant. Another important consequence

of Eq. 4.1 is that if the source resonator is substantially larger than the device and provided that the devices are sufficiently separated from one another (i.e. we are dealing with a "dilute" system of resonators), then the coupling between the source and each device dominates over the direct coupling between devices and allows us to derive exactly the optimal efficiency of a dilute system consisting of an arbitrary number of devices.

The bulk of the work for this project consisted of building a wireless power transfer setup comprising one large source $\sim$ 1 m^2 in area and two smaller devices $\sim$ 0.07 m^2 and experimentally verifying that the optimal efficiency of a system of two dilute devices behaves as predicted by the coupled-mode theory treatment. Because the areas of the source and device coils in this experiment are respectively four times and one-quarter of the area of the coils in Chap. 3, the optimal efficiency as a function of distance between the source and one device will be reasonably close to that obtained in the first experiment as expected from Eq. 4.1.

4.3 Coupled-mode theory for a dilute system of resonators

We once again employ the framework of coupled-mode theory, except that, instead of the variables Γ_m and κ_{mn} used in Eq. 3.1, we now work directly in terms of the dimensionless parameters $Q_m = \omega_m/[2\Gamma_m]$ (the quality factor of the resonator labeled by m and with resonant angular frequency ω_m) and $k_{mn} = 2\kappa_{mn}/\omega$ (the dimensionless coupling between resonators m and n), as these parameters are more familiar to large segments of the electrical engineering community which took an interest in our earlier work. The coupled-mode theory equations now read

$$\dot{a}_m(t) = -\left[i\omega_m + (1+x_m)\frac{1}{2Q_m}\right] a_m(t) + \frac{1}{2}\sum_{n\neq m} i\omega k_{mn} a_n(t) + F_m(t), \qquad (4.2)$$

where, as before, the complex-valued mode variables $a_m(t)$ are normalized so that the energy contained in resonator m is $|a_m(t)|^2$, x_m is the normalized external load-

ing that extracts the energy stored in mode m so it can be converted into useful work, and $F_m(t)$ is the external driving term. In the general case, finding a solution to Eq. 4.2 involves inverting an $M \times M$ matrix (M being the total number of resonators involved), which can lead to a wide range of interesting effects such as energy hopping [26]. This variety of possible phenomena also precludes the possibility of making precise statements about the optimal efficiency of an arbitrary system of mutually interacting resonators. Thankfully, the dilute approximation that we employ here—and which, as we argued, could be applied to potentially viable real-world applications—does admit an exact analytical solution for the efficiency and for the optimal loading parameters x_m. For definiteness, we label the (single) source resonator 0 [so that in Eq. 4.2, $F_0(t)$ is the only non-trivial driving term] and the N devices by $m = 1, 2, \ldots, N$. In the dilute case, the source is much larger than the devices and the devices are not particularly clustered together so that, by virtue of Eq. 4.1, the mutual coupling between devices is much smaller than the direct coupling between the source and each device. We therefore neglect all off-diagonal terms in Eq. 4.2 except for $k_{0m} = k_{m0}$. In the harmonic case $a_m(t) \sim e^{-i\omega t}$, Eq. 4.2 can be written in matrix form as

$$\mathbf{K}\left(\{\delta_m\}, \{Q_m\}, \{x_m\}, \{k_{0,m}\}\right) \cdot \begin{pmatrix} a_0 \\ a_1 \\ \vdots \\ a_N \end{pmatrix} = \begin{pmatrix} F_0 \\ 0 \\ \vdots \\ 0 \end{pmatrix}, \tag{4.3}$$

where $\delta_m = (\omega_m - \omega_m)/\omega_m$ is the fractional detuning of each coil from its resonant frequency. By inspection of Eq. 4.3, one can see that instead of fully inverting the matrix $\mathbf{K}$, we only need to find the first row of $\mathbf{K}^{-1}$ to determine all of the coupled-mode theory variables a_m. Using the adjoint method for matrix inversion, we find

that

$$|a_0|^2 = \left|\prod_{n=1}^{N}\omega_n\left[\frac{(1+x_n)}{2Q_n}+i\delta_n\right]\right|^2 \times \left|\frac{F}{\det\mathbf{K}}\right|^2 \tag{4.4}$$

$$|a_m|^2 = \frac{(\omega/\omega_m)^2 k_{0,m}^2 Q_m^2}{(1+x_m)^2+4Q_m^2\delta_m^2} \times \left|\prod_{n=1}^{N}\omega_n\left[\frac{(1+x_n)}{2Q_n}+i\delta_n\right]\right|^2 \times \left|\frac{F}{\det\mathbf{K}}\right|^2, \text{ for } m = 1, 2, \cdots, N. \tag{4.5}$$

It follows from the definition of the unloaded Q of a resonator [$\omega \times$ (total energy stored) / (average power dissipated)] and from the interpretation of $|a_m|^2$ as the energy stored in resonator m that the power dissipated per resonator is $P_m = \omega|a_m|^2/Q_m$. The normalized loading parameters x_m effectively lower the intrinsic Q's of the resonators of the coils by a factor of $1/(1+x_m)$, and a fraction $x_m/(1+x_m)$ of the total power dissipated in a coil [which now equals $P_m = (1+x_m)|a_m|^2/Q_m$] can in principle be converted into useful work. Defining the overall efficiency η of the system as the ratio of the overall power delivered to all the loads to the total power dissipated in all the resonators, we find

$$\eta = \frac{\sum_{n=1}^{N}\omega x_n|a_n|^2/Q_n}{\omega|a_0|^2/Q_0+\sum_{n=1}^{N}\omega(1+x_n)|a_n|^2/Q_n} \tag{4.6}$$

$$= \frac{\sum_{n=1}^{N}(\omega/\omega_n)^2\left(k_{0,n}^2Q_0Q_n\right)/\left[(1+x_n)^2+4Q_n^2\delta_n^2\right]}{1+\sum_{n+1}^{N}(\omega/\omega_n)^2(1+x_n)\left(k_{0,n}^2Q_0Q_n\right)/\left[(1+x_n)^2+4Q_n^2\delta_n^2\right]}, \tag{4.7}$$

where we have used Eqs. 4.4 and 4.5 in going from the first to the second line. We find that a condition for optimizing the overall efficiency is that all the devices be resonant at the driving frequency ω_d. The overall efficiency then becomes

$$\eta = \frac{\sum_{n=1}^{N}\left[x_n/(1+x_n)^2\right]\left[k_{0,n}^2Q_0Q_n\right]}{1+\sum_{n=1}^{N}\left[1/(1+x_n)\right]\left[k_{0,n}^2Q_0Q_n\right]}. \tag{4.8}$$

Comparing Eqs. 3.2 and 4.8, we notice a significant similarity between the single-device efficiency and the multiple-device efficiency for a system of dilute devices. Moreover, we find again that the efficiency depends only on the strong-coupling pa-

rameters $k_{0,m}\sqrt{Q_0 Q_m}$. This parallel extends to the optimal values of the normalized loading parameters x_m that optimize the efficiency. To solve for the optimal x_m for $m = 1, 2, \ldots, N$, we can proceed by induction as follows: starting with the case of two devices Eq. 4.8 can be readily maximized as a function of two variables to yield $x_1 = x_2 = \sqrt{1 + k_{0,1}^2 Q_0 Q_1 + k_{0,2}^2 Q_0 Q_2}$ as the optimal loading parameters. Plugging this back into Eq. 4.8, we see that the two device resonators can effectively be viewed as one effective resonator with an enhanced strong-coupling parameter $\sqrt{k_{0,1}^2 Q_0 Q_1 + k_{0,2}^2 Q_0 Q_2}$. We can then reduce the analysis of Eq. 4.8 for three device resonators to our previously solved analysis of two device resonators by treating any two device resonators as one effective resonator and obtain for the optimal normalized loading parameters $x_1 = x_2 = x_3 = \sqrt{1 + k_{0,1}^2 Q_0 Q_1 + k_{0,2}^2 Q_0 Q_2 + k_{0,3}^2 Q_0 Q_3}$. We conclude again that the three device resonators act as one effective resonator with effective strong-coupling parameter $\sqrt{k_{0,1}^2 Q_0 Q_1 + k_{0,2}^2 Q_0 Q_2 + k_{0,3}^2 Q_0 Q_3}$. This procedure can be repeated up to some arbitrary number N of device resonators with optimal loading parameters

$$x_{\text{eff}} = x_1 = x_2 = \ldots = x_N = \sqrt{1 + \sum_{n=1}^{N} k_{0,n}^2 Q_0 Q_n}, \tag{4.9}$$

and effective strong-coupling parameter

$$U_{\text{eff}} = \sqrt{\sum_{n=1}^{N} k_{0,n}^2 Q_0 Q_n}. \tag{4.10}$$

The efficiency is then more concisely expressed as the single-device efficiency (Eq. 4.8) for U_{eff}

$$\eta = \frac{[x_{\text{eff}}/(1 + x_{\text{eff}})^2]\, U_{\text{eff}}^2}{1 + [1/(1 + x_{\text{eff}})]\, U_{\text{eff}}^2}, \tag{4.11}$$

which makes it much simpler to analyze the effect on the overall efficiency of adding additional device resonators. One can see that the plot of the optimal efficiency as a function of the effective strong-coupling parameters (Fig. 3-1) has an inflection point in the vicinity of $U_{\text{eff}} \simeq 1$ (more precisely, at $U_{\text{eff}} = \sqrt[4]{3}/\sqrt{2} \simeq 0.9306$). Thus,

this is the region in parameter space where the addition of extra resonators would have a larger impact on the efficiency. As an example, a single device interacting with the source with a strong-coupling parameter of 1 (which one could consider to be borderline strongly coupled) would have an optimal efficiency of approximately 17.2%. The addition of another device with the same strong-coupling parameter would increase the optimal efficiency to 26.8%, while four devices with the strong-coupling value of 1 would have an optimal efficiency of 38.2%. We therefore conclude that the approach of having one large source power multiple small devices distributed over a large volume may lead to acceptable overall efficiencies even in cases where the single device efficiencies are modest (e.g., worse than 20%). Note, however, that this improvement only applies if the devices are driven simultaneously. In case one were to split up the single system of one source and N devices into N systems comprising one device each, e.g., by using time-multiplexing (the source would cycle through the separate frequencies of operation of devices, each of which would be sufficiently distinct to prevent strong coupling to the other devices) or by frequency-multiplexing (the source would operate at a superposition of frequencies, one for each device), the overall efficiency would necessarily be a weighed average of the efficiencies of the N separate systems, and hence lower than the optimized simultaneous case studied here.

4.4 Experimental results

To demonstrate the principles outlined above experimentally, we built a large self-resonant coil [48] that would serve as a source for two smaller device coils, all designed to resonate at 6.5 MHz, which is in the range of optimal frequencies for this class of resonators [44] and also close to the ISM (Industrial, Scientific, and Medical [22]) band at 6.78 MHz. The source coil is a helix made of 4 turns of 1/2" copper pipe, 113 cm in diameter, and 20 cm in height. The two devices are made of 15.25 turns of 1/4" copper pipe, 30 cm in diameter and 18 cm in height. In real-life applications, a source coil of this size (spanning an area of approximately 1 m^2) could potentially be embedded in the walls or in the ceiling of a room, while the area of the devices is comparable

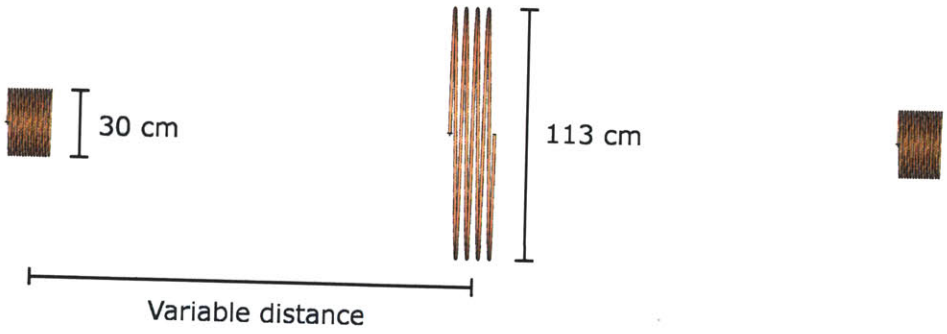

Figure 4-1: Computer-generated image of the experimental setup. For simplicity, the device coils are placed at identical distances on either side of the source (center coil). The image is to scale, with a center-to-center separation between the source and each device of 200 cm. In the laboratory, all coils were suspended by pieces of insulated string (which have no effect on the measurements) connected to the ceiling. The excitation and pickup coils are not shown.

to those of some portable electronic devices and domestic robots. We placed the devices on opposite sides of the source (Fig. 4-1). To couple and impedance-match to each resonator we used smaller loop-and-capacitor "coupling" coils tuned to the same frequency as the larger self-resonant coils (Fig. 4-2). Each coupling coil behaved to a good approximation as a standard RLC circuit, greatly simplifying the impedance matching procedure. The three coupling coils are then connected to appropriate driving and loading circuits by means of standard coaxial cables. In order to minimize the capacitive coupling of the self-resonant coils to the grounded sleeve of the coaxial cables, we aligned the excitation coils symmetrically with the mid-point of the helical coils.

By connecting each of the coupling coils to a separate port of a network analyzer and sweeping the driving frequency of the network analyzer around the resonant frequency of the self-resonant coils, it is possible to extract all of the coupled-mode theory parameters in Eq. 4.2 and Fig. 4-2 from a fit of the measured input impedances. We found experimentally that the quality factor of the source coil was $Q_0 = \omega/2\Gamma_0 =$

730 ± 50. Due to imperfections in their (manual) fabrication, the two device coils had somewhat different quality factors, with device coil 1 having $Q_1 = 1650 \pm 100$ and device coil 2 having $Q_2 = 1850 \pm 100$. The variation in the values of the quality factors was due in part to the systematic effect of having to manually retune the coils as they were moved to different positions, and in part due to uncertainties in the least-square fits through which the strong-coupling parameters were obtained.

In the approximation where the current distribution along the length of the self-resonant coils is a half-wave, we can apply the analytical model for self-resonant coils developed in section 3.4 to predict the coupling between the resonators as a function of distance. (In fact, before building the coils in the laboratory, the model was a valuable tool for estimating what the geometry of each coil should be.) Although this analysis does not take into account the imperfections of the coils, the calculated values are within 10% of the experimental values of k (Fig. 4-3), obtained in the same data fits as the experimental Q value. We found that the coupling $k_{0,2}$ between the source and the second device was consistently higher than $k_{0,1}$, a discrepancy that persisted even after we switched the positions of the two devices to control for a potential effect of the walls and extraneous metallic objects in the laboratory on the coupling between the resonators. We thus conclude that the difference in the coupling must is due to variations in the exact construction of the device coils (as were the differences in the quality factors of the two devices).

In order to effect power transfer at the resonant frequency, one can adjust the coupling between each coupling coil and its associated resonator by varying the distance between them or pitching the angle of the coupling coil, so that the system is properly matched to the 50 Ω ports of the network analyzer. After properly tuning the system, the efficiency can be directly measured by the network analyzer. We measured the efficiency between the source and each device separately, as well as the overall efficiency between the source and both devices simultaneously (Fig. 4-4). Note that, as a consequence of Eq. 4.9, the impedance-matching in the case of simultaneous devices differs from that of a single device. The directly matched efficiency at the optimal matching parameters matches the efficiency predicted from the coupled-mode theory

parameters derived from the fits to within 0.5%.

Once the matching is done with the help of a network analyzer, one can connect the coupling coils at the devices to a loading circuit with 50 Ω input impedance and drive the source with a 50 Ω RF amplifier to provide significant amounts of power to the devices. In our setup, we were able to supply upwards of 25 W to each device (the power being dissipated in resistive dummy loads) even when the devices were farther than 2 m from the source, the power level being constrained by the maximum output of the amplifier. Since RF amplifiers with efficiency greater than 90% are common [25], they have a minor effect on the wall-to-load efficiency, especially compared to the Colpitts oscillator used in Chap. 3.

It can be readily seen from Fig. 4-4 that the relative improvement in overall efficiency due to having two devices coupled simultaneously to the source (green) compared to having each device couple separately to the source (blue and red) is more significant when the devices are placed at longer distances from the source, i.e. when the coupling and strong-coupling parameters are lower, as predicted by our couple-mode theory analysis.

4.5 Conclusion and outlook

We have derived analytically and shown experimentally for the case of two devices the effect on the overall efficiency and on the optimal loading of the devices of adding multiple device resonators to a system of strongly-coupled resonant modes. We find that the approach of powering multiple devices simultaneously can result in a good overall efficiency for the wireless power transfer even if the efficiency of the transfer to each individual device is relatively low. Although the area of the self-resonant device coils in this chapter is one-quarter of the area of our original self-resonant coils (Chap. 3) and more comparable in dimension to the area of a wide range of electronic devices, their significant height (18 cm) presents a major difficulty to their seamless integration with existing equipment. Planar coils, in which the conductor is confined to a plane and spirals towards the center starting from some outer radius, would

present a much reduced profile (i.e. of the order of the diameter of the conductor from which the coil is formed), but our analytical model indicates that, for a fixed area and relative to helical coils, their coupling would be significantly reduced if the spiral terminates too close to the center (this can be be intuitively understood by noting that the inner turns of the spiral enclose a smaller area and therefore capture less of the magnetic field produced by another coil). An electrical conductor that offers similar resistance to the heavy gauge wires used up to now yet takes up a much smaller volume would go a long way towards resolving these issues. In the next chapter, we present a new design for an electrical conductor that meets these characteristics.

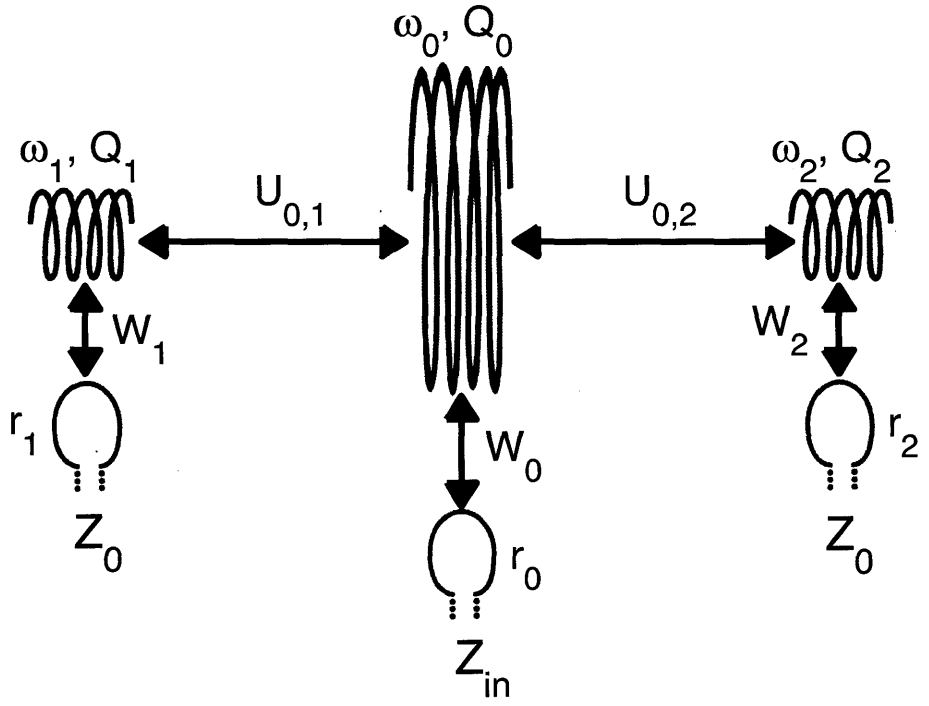

Figure 4-2: Schematic representation of the experimental setup showing all the quantities of relevance to a coupled-mode theory analysis of the system and to the impedance-matching to three ports of a network analyzer. The source coil is at the center (compare to Fig. 4-1). The angular resonant frequencies and quality factors of each resonator are shown above the respective self-resonant coils. $U_{0,1}$ and $U_{0,2}$ are the strong coupling parameters between the self-resonant coils (the cross-coupling $U_{1,2}$ being negligible by comparison). Also shown are the strong-coupling parameters W_0, W_1, and W_2 between each self-resonant coil and its coupling coil, the series resistance (r_0, r_1, and r_2) of each coupling coil, the input impedance seen by the source port of the network analyzer and the output impedance of the device ports of the network analyzer ($Z_0 = 50\ \Omega$). All of the parameters shown can be extracted from the data measured by the network analyzer.

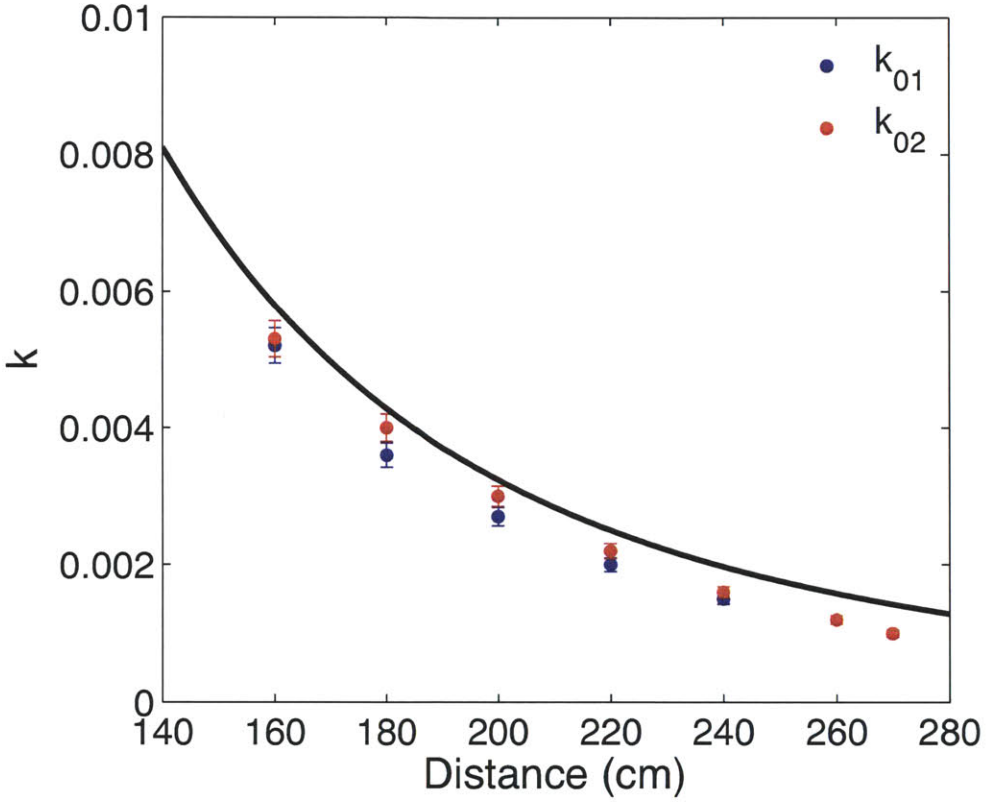

Figure 4-3: Coupling $k = 2\kappa/\omega$ between the source and each device as a function of center-to-center distance. Because of imperfections in the fabrication of the device coils, the measured coupling at the same distance for the two devices (blue and red) differs by $\sim 10\%$. Since $\sqrt{Q_0 Q_{1,2}} \simeq 1100$, each device is strongly coupled to the source ($k\sqrt{Q_0 Q_{1,2}} > 1$) over the entire range of distances. Also plotted is the coupling predicted (black) by a simple (and relatively easy to calculate) model that ignores the imperfections of the coils, but nevertheless gives predictions within 10% of the measured results.

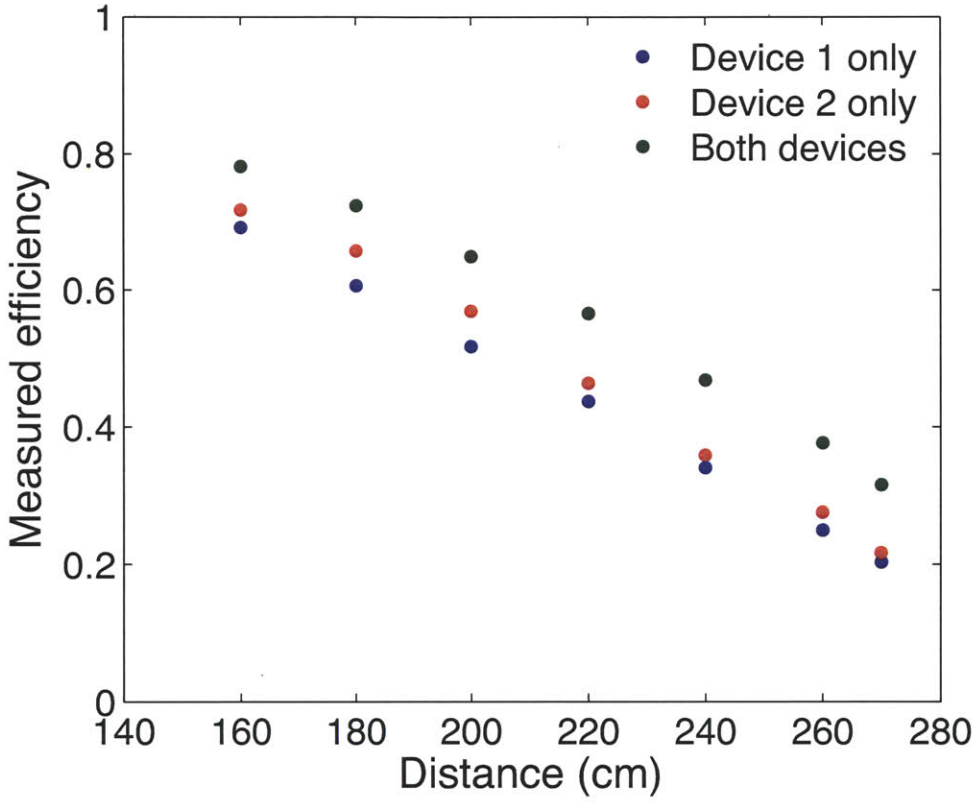

Figure 4-4: Efficiency as a function of distance for the cases where each device alone is coupled to the source and where both devices are coupled simultaneously to the source, and properly matched according to Eq. 4.9. The losses due to the small resistance of the coupling coils have been subtracted out. Because of differences in the construction of the devices, their Q's and coupling to the source (see Fig. 4-3) are different, thereby leading to a somewhat higher efficiency for device 2.

Chapter 5

A low-resistance electrical conductor for the multi-MHz range

5.1 Summary

We propose a new design for a conductive wire composed of several mutually insulated coaxial and conducting shells. With the help of numerical optimization, it is possible to obtain electrical resistances significantly lower than those of a heavy-gauge copper wire or litz wire (the best currently available alternatives) in the 2–20 MHz range. Moreover, much of the reduction in resistance can be achieved for just a few shells; in contrast, litz wire would need to contain $\sim 10^4$ strands to perform comparably in this frequency range. Although the original motivation for this work was to create a conductor that would significantly improve the performance of high-Q coils for midrange wireless power transfer and to facilitate their miniaturization and integration with portable devices, our results could also be pertinent to a number of other uses such as RFID or applications operating at the ISM frequency bands at 6.78 and 13.56 MHz [22].

5.2 Overview

In this chapter, we show that a structure of concentric cylindrical conducting shells can be designed to have much lower electrical resistance for $\sim$ 10 MHz frequencies than heavy gauge wire or available litz wires. At such frequencies, resistance is dominated by skin-depth effects, which forces the current to flow within approximately one skin-depth δ (which is $\simeq$ 20 μm for copper at 10 MHz) of the surface of the conductor, rather than being uniformly distributed over the cross section. As a result, the electrical resistance at radio-frequencies scales inversely with the linear dimension of the cross-section of the conductor, rather than as the inverse of the cross-sectional area characteristic of direct-current (DC) resistance. The skin-depth effect is typically mitigated by breaking the wire into a braid of many thin insulated wires (litz wire [76, 24, 57]), but the short skin depth at these frequencies makes traditional litz wire impractical, as they would need to be composed of $\sim$ 10^4 μm-scale strands. In contrast, we show that, in the case of a cylindrical conductor with cross-sectional diameter 1 mm, as few as 10 coaxial shells can improve resistance by more than a factor of 3 compared to solid wire, and thin concentric shells can be fabricated by a variety of processes (such as electroplating, electrodeposition, or even a fiber-drawing process [6, 50, 18]). We derive an analytical expression for the impedance matrix of both litz wire and nested cylindrical conductors starting from the quasistatic Maxwell equations; in particular, a key factor turns out to be the proximity losses [49] induced by one conductor in another conductor via magnetic fields. Using this result combined with numerical optimization, we are able to quickly optimize all of the shell thicknesses to minimize the resistance for a given frequency and number of shells. As a check of our analytical results, we also perform finite-element method simulations for both litz wire and concentric shell structures.

For a cylindrically symmetrical system of nested conductors oriented along the z direction, we shall see that Maxwell's equations reduce to a Helmholtz equation in each annular layer. In the quasistatic limit of low frequency (which causes the conductivity term to dominate over the dielectric constant), we show that this further

simplifies into a scalar Helmholtz equation for E_z alone, which can be solved in terms of Bessel functions. The coefficients of these Bessel functions are determined by the boundary conditions at each interface: continuity of E_z and of $H_\phi \sim \partial E_z/\partial r$. Once the solution for E_z, and thus the current density σE_z (for conductivity σ) and the magnetic fields (from Ampere's law), are obtained, the impedance matrix can be derived from energy considerations. Of course, a real wire is not perfectly cylindrical because of bending and other perturbations, but these effects can typically be neglected to good approximation (e.g., if the bending radius is much larger than the wire radius).

5.3 Analytical procedure

We start by analytically solving Maxwell's equations in each medium (air, copper, and insulator):

$$\nabla^2 \mathbf{E}(\mathbf{r}) + \left(k^2 + 2i\kappa^2\right) \mathbf{E}(\mathbf{r}) = 0. \tag{5.1}$$

Here $k = \sqrt{\epsilon_r}\omega/c$, ω is the angular frequency, ϵ_r is the relative permittivity, c is the speed of light in vacuum, $\kappa = 1/\delta = \sqrt{\omega\mu_0\sigma/2}$ (δ is commonly called the skin depth [49]), μ_0 is the magnetic constant, and σ is the conductivity (5.9×10^7 S/m for copper, zero otherwise). Since the wavelength ($\lambda = 2\pi/k \simeq 15$ m in vacuum at 20 MHz) is much longer than the conductor thickness or the skin depth, the k^2 term in Eq. 5.1 is negligible for solving within a given cross-section z. Under these approximations, the z–component of Eq. 5.1 becomes

$$\frac{\partial^2 E_z(r,\phi)}{\partial r^2} + \frac{1}{r}\frac{\partial E_z(r,\phi)}{r} + \frac{1}{r^2}\frac{\partial^2 E_z(r,\phi)}{\partial \phi^2} + 2i\kappa^2 E_z(r,\phi) = 0, \tag{5.2}$$

which can be solved by separation of variables. The general solution $E_z(r,\phi)$ of Eq. 5.2 in the conductor has the form

$$E_z(r,\phi) = \sum_{m=0}^{\infty} \left[A_m J_m(\eta) + B_m Y_m(\eta)\right] \left[C_m \cos(m\phi) + D_m \sin(m\phi)\right] \tag{5.3}$$

where $J_m(\eta)$ and $Y_m(\eta)$ are Bessel functions, and $\eta = \sqrt{2i}\kappa r$. The magnetic field can then be found through Faraday's law: $i\omega B_\phi = \partial E_z/\partial r$. The constants A_m, B_m, C_m, and D_m are determined by continuity of E_z and H_ϕ at interfaces, and by using Ampere's law to relate a line integral of the magnetic field around a conductor to the enclosed current. Equivalently, we could have replaced $J_m(\eta)$ and $Y_m(\eta)$ in Eq. 5.3 with the Hankel functions $H_m^{(\pm)}(\eta) = J_m(\eta) \pm iY_m(\eta)$, which are sometimes more numerically convenient. Finiteness at $r = 0$ dictates that the innermost layer must have $E_z(\eta) \sim J_m(\eta)$. Given a set of N conductors, one can find the impedance matrix by first using the procedure above to solve for the electric and magnetic fields associated with the N distinct cases where a single conductor k ($k = 1, 2 \ldots, N$) carries a net current $I_k \exp(i\omega t)$. The impedance matrix can then be derived by enforcing conservation of energy [49]. For example, one can find the complex-symmetric impedance matrix $Z_{k,l}$ by exciting the elements with currents $I_k \exp(i\omega t)$, superposing the previously computed solutions for the electric and magnetic fields, and computing the (complex) energy U of the system by integrating the net Poynting flux $\mathbf{S} = \mathbf{E} \times \mathbf{H}^*/2$ flowing into each shell and integrating the magnetic energy density $\mathbf{B} \cdot \mathbf{H}^*/4$ elsewhere. $Z_{k,l}$ then follows from $U = \sum_{k,l} I_k Z_{k,l} I_l^*/(2i\omega)$. Once the impedance matrix is known, it is straightforward to compute the power dissipated by any currents $I_k \exp(i\omega t)$: $P_{\text{dis}} = \sum_{k,l} \text{Re}\{I_k Z_{k,l} I_l^*\}/2$. Since the total current is $\sum_k^N I_k \exp(i\omega t)$, the overall resistance is

$$R = \text{Re}\left\{\sum_{k,l=1}^{N} I_k Z_{k,l} I_l^*\right\} \Bigg/ \left|\sum_{k=1}^{N} I_k\right|^2 . \tag{5.4}$$

Alternatively, if the current distribution is known beforehand (as in litz wire), one can compute the power dissipated and thus the overall resistance of the system by solving for the fields and integrating the Poynting flux into each conductor without computing Z.

5.4 Analytical treatment of a litz wire

We begin by reviewing traditional litz wire. It is convenient to split the problem into two steps: we first solve Eq. 5.2 for an isolated cylindrical strand of diameter d carrying current I_{strand}, and then consider the proximity effect on a single strand from the net magnetic field of all strands. The first step is cylindrically symmetric, and the electric and magnetic fields in the interior of the wire and the power dissipated per length are respectively

$$E_z(r) = \left(\frac{2}{\pi d^2 \sigma}\right)\left[\eta_s \frac{J_0(\eta)}{J_1(\eta_s)}\right] I_{\text{strand}}, \tag{5.5}$$

$$H_\phi(r) = \left(\frac{1}{\pi d}\right)\left[\frac{J_1(\eta)}{J_1(\eta_s)}\right] I_{\text{strand}}, \tag{5.6}$$

$$P_{\text{own}} = \left(\frac{1}{\pi d^2 \sigma}\right) \text{Re}\left\{\eta_s \frac{J_0(\eta_s)}{J_1(\eta_s)}\right\} |I_{\text{strand}}|^2, \tag{5.7}$$

where $\eta_s = \sqrt{2i}\kappa d/2$. If there are N identical strands carrying identical currents adding up to a total current $I = N \times I_{\text{strand}}$, and uniformly arranged into a circular bundle of overall diameter D, then the magnitude of the total internal magnetic field at a radius R from the center of the bundle is well approximated by

$$|\mathbf{H}_{\text{int}}(R)| = 2IR/(\pi D^2). \tag{5.8}$$

If $d/D \ll 1$, $|\mathbf{H}_{\text{int}}|$ is essentially uniform over each strand, in which case the induced fields and induced power dissipated (the "proximity loss") in a strand subjected to the overall field $|\mathbf{H}_{\text{int}}|$ are

$$E_z(r,\phi) = \left(\frac{2}{a\sigma}\right)\left[\eta_s \frac{J_1(\eta)}{J_0(\eta_s)}\right] |\mathbf{H}_{\text{int}}| \sin(\phi) \tag{5.9}$$

$$H_\phi(r,\phi) = \left[\frac{J_2(\eta) - J_0(\eta)}{J_0(\eta_s)}\right] |\mathbf{H}_{\text{int}}| \sin(\phi) \tag{5.10}$$

$$P_{\text{prox}} = \left(\frac{\pi}{\sigma}\right) \text{Re}\left\{\eta_s \frac{J_1(\eta_s)\left[J_2(\eta_s) - J_0(\eta_s)\right]^*}{|J_0(\eta_s)|^2}\right\} |\mathbf{H}_{\text{int}}|^2 \tag{5.11}$$

where the angle ϕ is measured relative to the direction of $\mathbf{H}_{\text{int}}$. Because the two sets of solutions described by Eqs. 5.5–5.6 and 5.9–5.10 are orthogonal in ϕ, there are no additional loss mechanisms due to interference between the two solutions and we can compute the overall power dissipated in the litz wire by summing the computed losses due to the strands carrying a net current (Eq. 5.7) and to the proximity losses (Eq. 5.11). The former are simply N times Eq. 5.7 (keeping in mind that $I_{\text{strand}} = I/N$). To compute the proximity losses, we would in principle need to evaluate $|\mathbf{H}_{\text{int}}|$ at the position of each strand and plug it into Eq. 5.11. Because of our assumption that the strands are uniformly distributed in the bundle and that $N \gg 1$, we can substitute the sum over the position of all strands by an integral over the cross-section of the bundle and substitute $|\mathbf{H}_{\text{int}}|^2$ in Eq. 5.11 by its average $\left[|\mathbf{H}_{\text{int}}|^2\right]_{\text{ave}} = |I|^2/(2D^2)$. Adding up the losses from all the strands we find that the resistance per length of a litz wire is (ignoring a small correction from the finite strand-winding pitch due to the braiding of the strands)

$$R_{\text{litz}} = \frac{2}{N\pi d^2\sigma}\text{Re}\left\{\eta_s\frac{J_0(\eta_s)}{J_1(\eta_s)}\right\} + \frac{N}{\pi D^2\sigma}\text{Re}\left\{\frac{\eta_s J_1(\eta_s)\left[J_2(\eta_s) - J_0(\eta_s)\right]^*}{|J_0(\eta_s)|^2}\right\}. \quad (5.12)$$

In the limit $\kappa d \ll 1$, we can expand the Bessel functions in Eq. 5.12 to find the lowest-order deviation from the DC resistance of N strands $[4/(N\pi d^2\sigma)]$:

$$R_{\text{litz}} \simeq \left(\frac{4}{N\pi d^2\sigma}\right)\left[1 + \frac{1}{128}\left(\frac{Nd}{D}\right)^2(\kappa d)^4\right]. \quad (5.13)$$

Thus, to keep the resistance near the DC resistance of a solid conductor of diameter D $[4/(\pi D^2\sigma)]$, one would need the scalings $N \sim 1/d^2$ and $d \sim 1/\kappa^2 \sim 1/\omega$. For example, with $D = 1$ mm at 10 MHz, one would need about $N \simeq 10^4$ strands and $d < 10\,\mu$m diameters in order to have a total resistance within a factor of 3 of the target value. As we shall see next, common commercially available litz wires ($\sim 10^2$ strands per mm^2) would typically perform significantly worse than a solid copper wire of the same overall diameter in this frequency range.

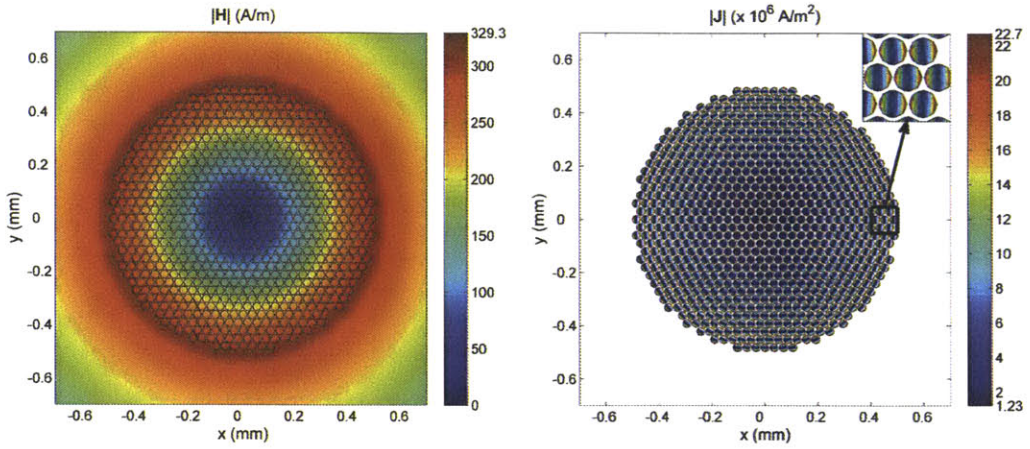

Figure 5-1: Results of the finite-element modeling (FEM) of a litz wire with overall cross-sectional diameter 1 mm and comprising 745 individual AWG 48 strands (strand diameter $d = 31.6$ μm). The litz wire carries an overall current of 1 A into the page and the solution shown is for a frequency of 10 MHz. The image on the left shows the magnitude of the magnetic field generated by the electrical current flowing through the strands, which closely follows Eq. 5.8. The panel on the right shows the magnitude of the current density in the strands. The induced current density manifests itself as the significant non-uniformity of the current density over the cross section of the strands (inset). Note that the induced currents become more significant closer to the surface of the bundle, where the magnetic field is strongest.

5.5 Finite-element modeling of a litz wire

In order to check the validity of our derivation of Eq. 5.12, we performed a finite-element analysis [13] of a litz wire (Fig. 5-1) of overall diameter $D = 1$ mm made of 745 uniformly distributed strands of diameter $d = 31.6$ μm [corresponding to American Wire Gauge (AWG) 48, the thinnest strands commonly used in litz wire [58]]. Fig. 5-2 compares the resistance per length of this litz wire to a solid copper wire of same overall dimensions. Although the litz wire has an initial advantage at 1 MHz, the resistance of the copper pipe increases approximately as $\sim \sqrt{\omega}$ while the resistance of the litz wire initially increases as $\sim \omega^2$ (because of Eq. 5.13) and–despite its complexity–the litz wire delivers considerably worse performance than the solid conductor above 5 MHz. Also of note in Fig. 5-2 is the good agreement between the

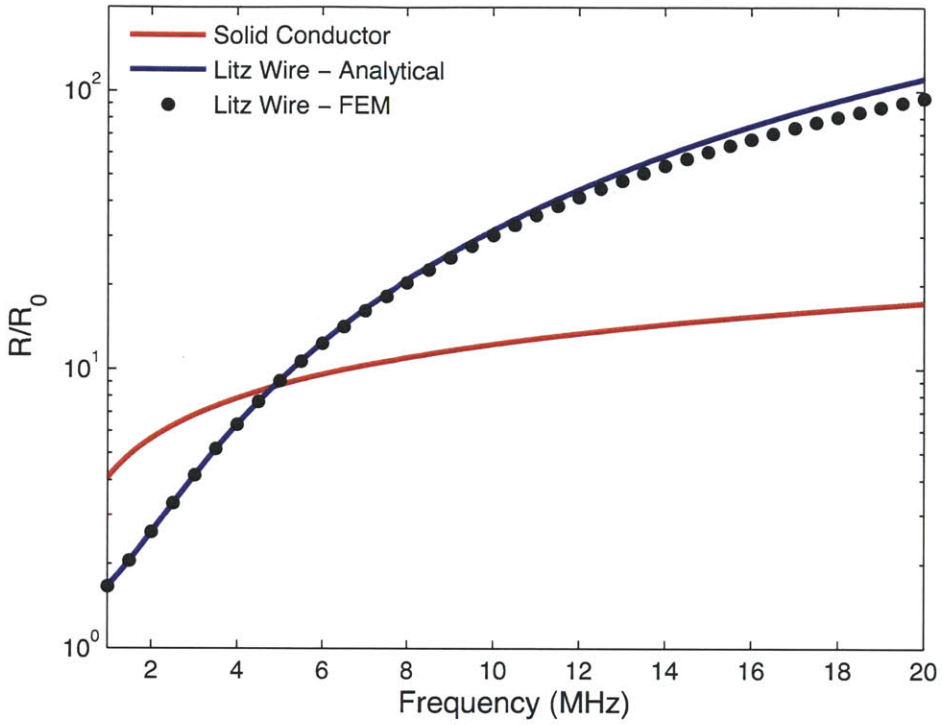

Figure 5-2: Semi-logarithmic plot comparing the resistances as a function of frequency of a solid copper conductor of diameter 1 mm and the litz wire from Fig. 5-1. The resistances are normalized to the DC resistance of the solid copper conductor (21.6 mΩ/m). The resistance of the litz wire is computed using both the analytical model derived in the text (Eq. 5.12) and a full FEM analysis.

finite-element modeling (FEM) and analytical results (in spite of the simplifications made in the deriving the latter), especially at frequencies below 10 MHz. The discrepancy between the two models widens as the frequency increases, and is $\simeq 20\%$ at 20 MHz. Closer inspection of the FEM models shows that the considerable induced currents at higher frequencies cause a substantial deviation of the magnitude of the magnetic field from the form assumed in Eq. 5.8. Although our analytical litz wire model could be suitably modified to be more accurate at higher frequencies by introducing higher order terms to the internal magnetic field, there may be little practical benefit in doing so considering the poor performance of a litz wire compared to the much simpler solution of a solid conductor in this regime.

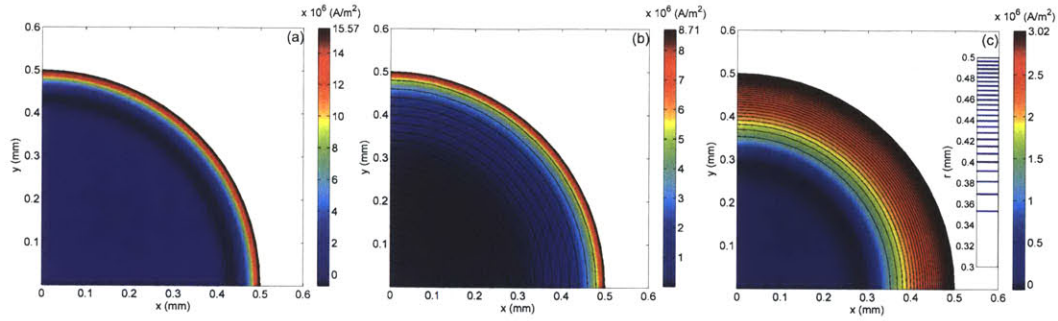

Figure 5-3: Optimal current density at 10 MHz for a copper conductor with diameter 1 mm when the wire consists of: (a) one piece of copper (resistance per length of 265.9 mΩ/m), (b) 25 mutually insulated conductive concentric shells of equal thickness 20 μm (148.7 mΩ/m), and (c) 25 elements whose thicknesses are optimized so as to minimize the overall resistance (51.6 mΩ/m). In (c), the inset shows the radial locations (blue) of the interfaces between shells. The overall current is 1 A. For simplicity, the insulating gap between shells is taken to be negligibly small. These geometries were solved analytically in the text, whereas these images were generated by a finite-element method [13] as a check. The color scales of the images are distinct for the sake of readability.

5.6 Solution of a coaxial and conducting shell structure

We now consider concentric shells and solve for the electromagnetic fields when shell k is excited by a current $I_k \exp(i\omega t)$. This scenario can be reduced to two cases: a shell carrying a current with no external field and a shell carrying no net current but immersed in a magnetic field H_ϕ generated by a current-carrying inner shell. In either case, the solutions are determined by continuity and by the fact that the magnetic field in a non-conductive medium at a radius r is $H_\phi = I/(2\pi r)$, where I is the total current inside the radius r. For a shell with inner radius a, outer radius b, and carrying current I, the fields are then:

$$E_z(\eta) = \frac{\sqrt{2i}\kappa I}{2\pi\sigma}\left[C_{a,b}^{(+)}H_0^{(+)}(\eta) + C_{a,b}^{(-)}H_0^{(-)}(\eta)\right] \tag{5.14}$$

$$H_\phi(\eta) = \frac{I}{2\pi}\left[C_{a,b}^{(+)}H_1^{(+)}(\eta) + C_{a,b}^{(-)}H_1^{(-)}(\eta)\right], \tag{5.15}$$

where the constants $C_{a,b}^{(\pm)}$ are given by

$$C_{a,b}^{(\pm)} = \frac{\mp H_1^{(\mp)}(\eta_a)/b}{H_1^{(+)}(\eta_a)H_1^{(-)}(\eta_b) - H_1^{(+)}(\eta_b)H_1^{(-)}(\eta_a)}, \tag{5.16}$$

with $\eta_a = \sqrt{2i}\kappa a$ and $\eta_b = \sqrt{2i}\kappa b$. Similarly, for the case of a shell with no current but enclosing a total current I, the fields are identical to Eqs. 5.14 and 5.15 except that $C_{a,b}^{(\pm)}$ are replaced by

$$D_{a,b}^{(\pm)} = \frac{\mp \left[H_1^{(\mp)}(\eta_a)/b - H_1^{(\mp)}(\eta_b)/a\right]}{H_1^{(+)}(\eta_a)H_1^{(-)}(\eta_b) - H_1^{(+)}(\eta_b)H_1^{(-)}(\eta_a)}. \tag{5.17}$$

As in the analysis of litz wire, we also conducted FEM simulations of various concentric shell structures. Since the solutions in this section are exact, they agree with the FEM results up to numerical accuracy, and the latter serve mostly as a consistency check of our derivations.

5.7 Optimization of a coaxial and conducting shell structure

Now that we know the analytical solution to an arbitrary system of concentric shells, it is straightforward to derive the full impedance matrix, as described previously, to compute the resistance of any given current distribution via Eq. 5.4. A uniform current distribution over N shells of equal thickness t, for instance, would have losses similar to those of a litz wire, although with a much smaller number of components ($N \sim \sqrt{N_{\text{strands}}/\pi}$, where N_{strands} is for a litz wire with $d = t$). Given that the exact impedance matrix is known, elementary calculus yields the currents I_k that minimize Eq. 5.4 [Fig. 5-3(b) shows an exemplar current distribution]. A more dramatic reduction in the resistance, especially when $N \sim \kappa D$, comes from letting the inner and outer radii of each shell vary (allowing the impedance matrix to vary) and then minimizing Eq. 5.4 using numerical optimization (more precisely, the COBYLA

algorithm [64] implemented in a freely available software package [39]) [Fig. 5-3(c)]. Fig. 5-4 compares the lowest resistance (as a function of N and the frequency) achievable by fixing the overall diameter of the conductor at $D = 1$ mm and optimizing both the dimensions of the individual shells and the current distribution to the resistance of a solid, heavy-gauge, conductor (typically the best currently available solution as shown in Fig. 5-2) of the same overall D [resistance/length $\simeq \kappa/(\pi D\sigma)$ for $\kappa D \gg 1$], while Fig. 5-5 compares it to the DC resistance per length of a solid copper wire $[4/(\pi D^2\sigma)]$ (which corresponds to the $N \to \infty$ limit where proximity losses vanish and the current flows uniformly over the cross section). Fig. 5-6 compares the optimized coaxial shell structure to the best resistance achievable with a structure consisting of N shells of *equal* thickness, illustrating the significant improvements that can be obtained with optimization of the geometry of the structure, even while the total number of shells is fixed.

5.8 Conclusion and outlook

A potential disadvantage of a concentric-shell structure compared to traditional litz wire is that the braiding of the latter automatically takes care of the problem of impedance-matching. However, one can see from Figs. 5-4 and 5-7 that much of the relative improvement of an optimized concentric shell conductor over a solid conductor occurs for structures with only a handful of elements, where even a brute force approach of individually matching the impedance of each shell to achieve the optimal current distribution could be implemented. As shown in Fig. 5-7, an optimized concentric shell conductor with 10 elements and overall diameter 1 mm would have roughly 30% of the resistance of a solid conductor of the same diameter over the entire 2–20 MHz range. Equivalently, since the resistance of a solid conductor in the regime $\kappa D \gg 1$ scales as $1/D$, our optimized conductor with ten elements would have the same resistance per length as a solid conductor with a diameter $\sim 1/0.3 \simeq 3.33$ times greater (and $\simeq 10$ times the area). Considering specific applications to high-Q resonators for midrange wireless power transfer, our results suggest that it should be

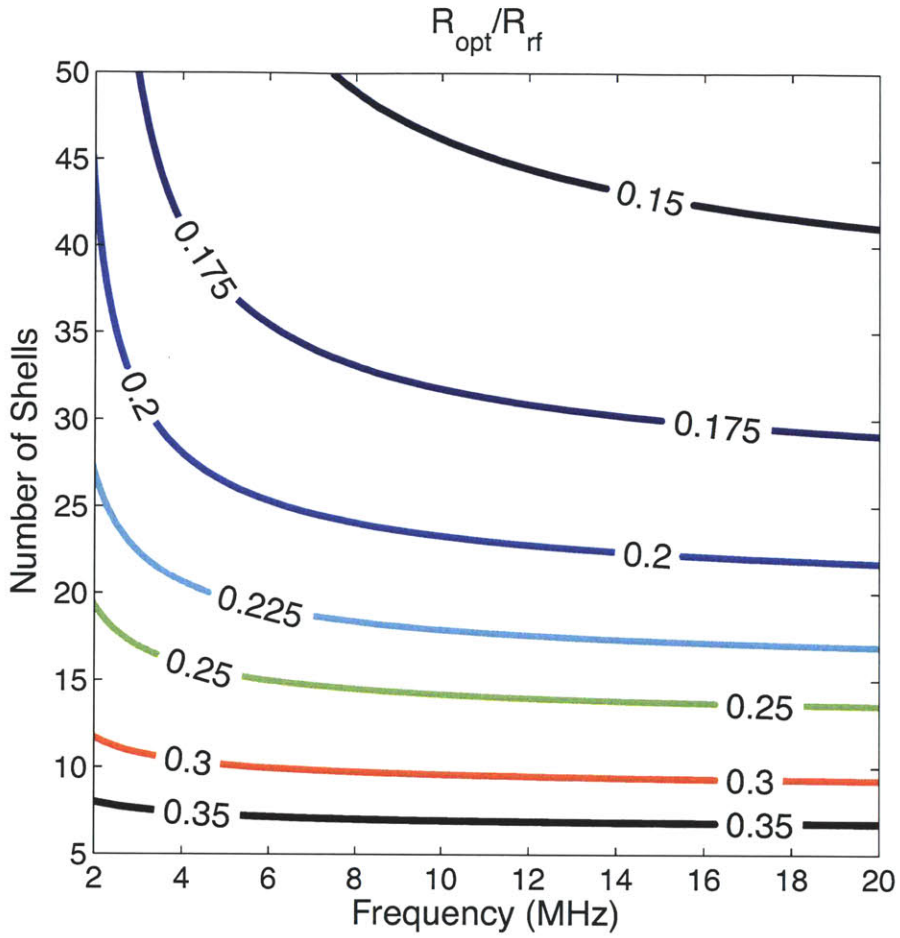

Figure 5-4: Ratio of the resistance per length of an optimized conducting-shell structure with overall diameter 1 mm to that of a solid conductor of the same diameter (Fig. 5-2).

possible to build resonators with height $\sim$ 1 mm and performance similar to those of the device coils in Chap. 4.

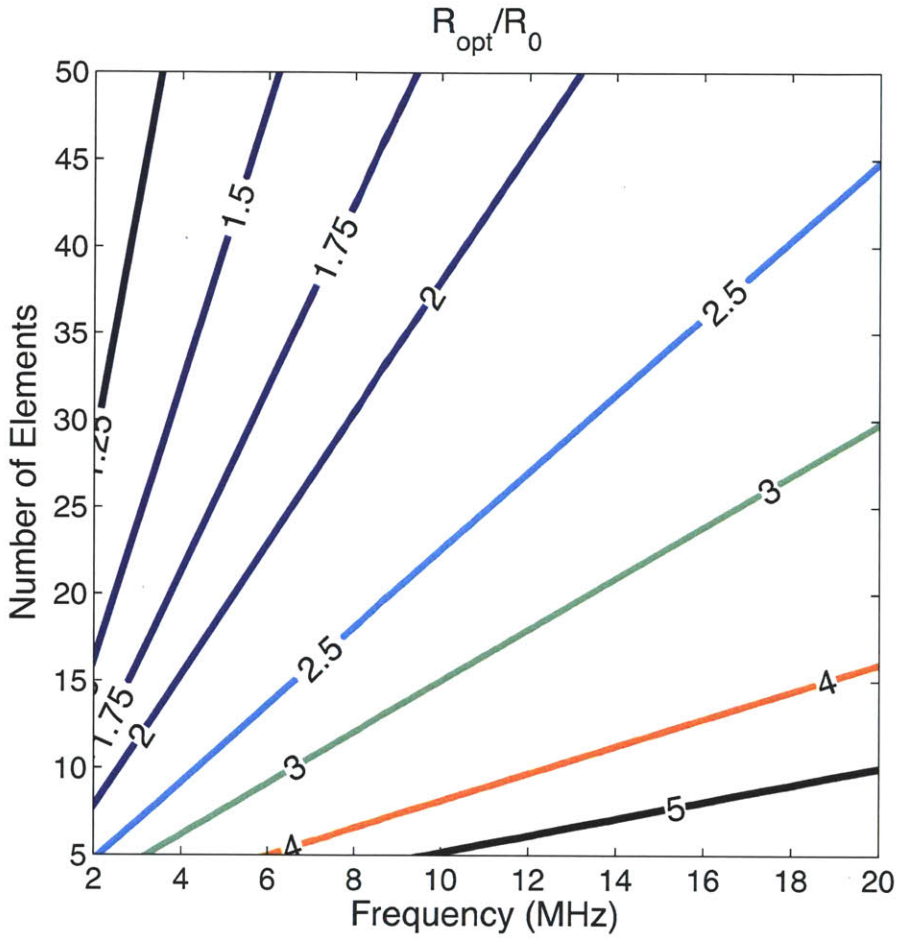

Figure 5-5: Ratio of the resistance per length of an optimized conducting-shell structure to the DC resistance per length of a cylindrical copper conductor of same diameter 1 mm. As $N \to \infty$, the quantity plotted asymptotes to 1.

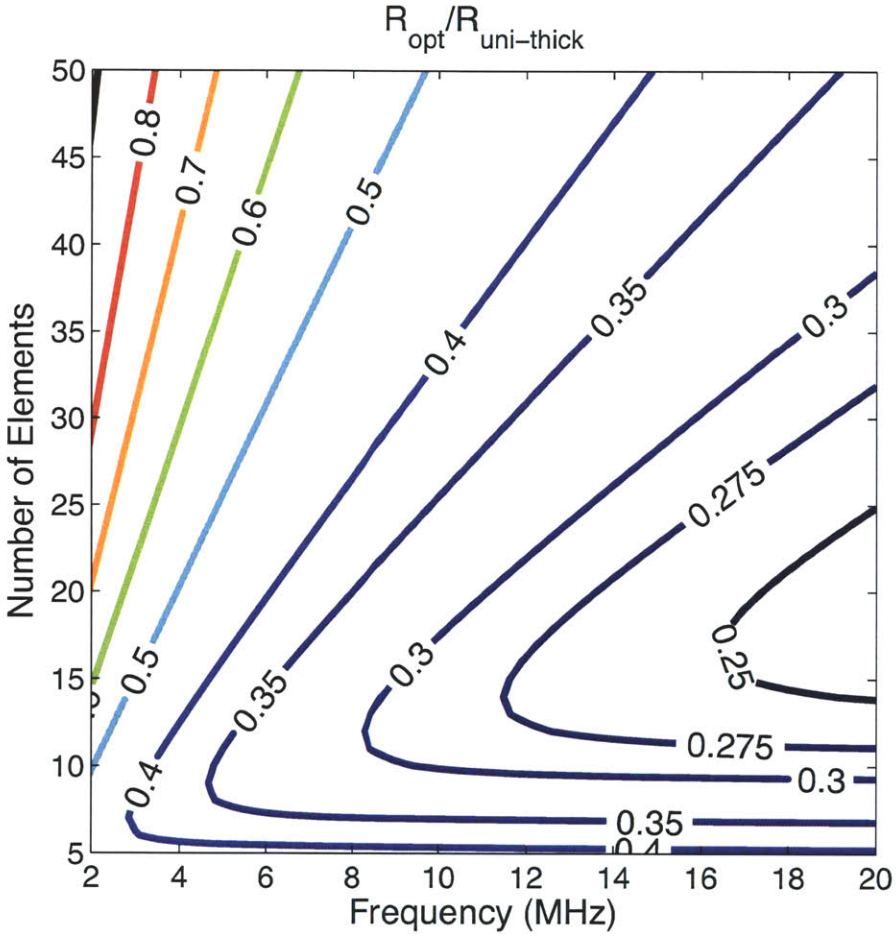

Figure 5-6: Ratio of the resistance per length of an optimized conducting-shell structure with overall diameter 1 mm to that of a conducting-shell structure (of same overall dimensions) comprising the same number of shells but of uniform thickness (not optimized) [Fig. 5-3(b)].

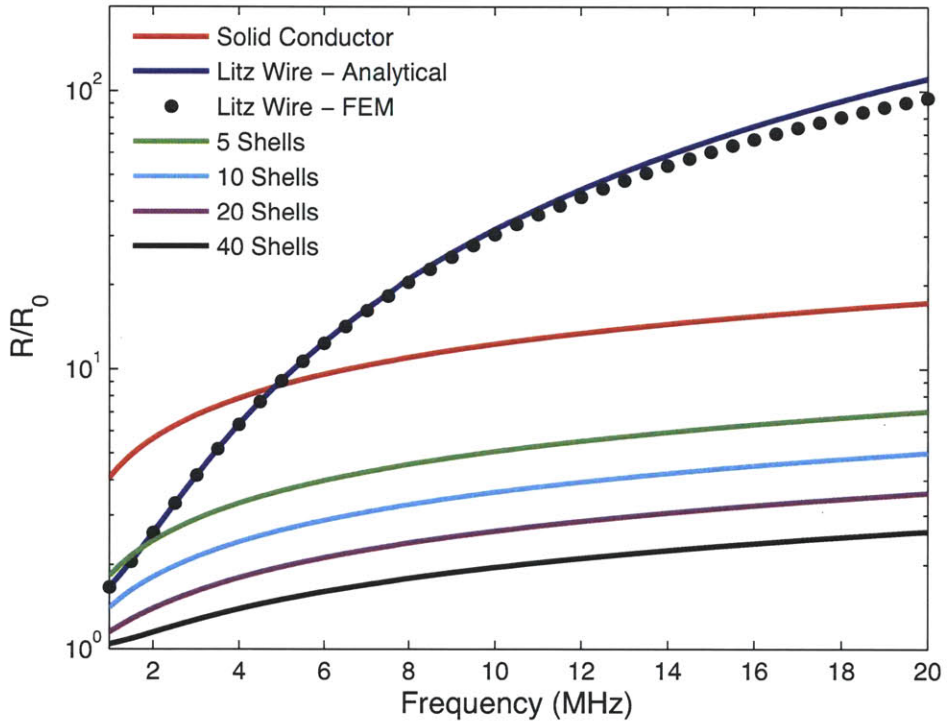

Figure 5-7: Semi-logarithmic plot comparing the resistances per length (normalized to the DC resistance per length of a solid copper conductor of same diameter 1 mm) for a few optimized coaxial structures of increasing complexity. For reference, the resistances per length of a solid conductor and the previously discussed litz wire (Fig. 5-2) are also shown.

Chapter 6

Supercollimation in a slab of silicon rods

6.1 Summary

In this chapter we present our key contributions to a collaborative project that led to the first experimental demonstration of supercollimation in a photonic crystal slab composed of nanoscale rods. Using numerical simulations of the photonic crystal and informed by the constraints of the fabrication process, we helped define the final dimensions of the structure that was fabricated for the experiment. We also analyzed how well a supercollimating photonic crystal would perform as a chemical sensor, and explored how the supercollimation length would be affected by the frequency of operation.

6.2 Overview

Among the rich variety of phenomena [83, 38, 37] enabled by photonic crystals, supercollimation enables the propagation of a light beam inside a photonic crystal with nearly no diffraction [45]. Much of the recent work on supercollimation has focused on photonic crystals composed of periodic arrays of air holes in a dielectric slab [46, 81, 84, 3, 66, 65]. Here, we focus instead on a periodic structure of rods in air.

The basic strategy for achieving supercollimation is the same regardless of the particulars of the photonic crystal: solve for the photonic band structure and look for equifrequency contours with flat sections. The group velocity vectors $\mathbf{v}_g = \partial\omega/\partial\mathbf{k}$ for the electromagnetic modes lying along such a flat section point substantially in the same direction, leading to a dramatic reduction in the diffraction of a beam composed of such modes. The degree of supercollimation achievable for a given contour can estimated quantitatively using a two-dimensional beam propagation method (BPM) based on the paraxial approximation [14, 5], and we use this model to compare the frequency bandwidth of supercollimation in the rod structure to that of a previously demonstrated photonic crystal hole slab [66]. Finally, we use perturbation theory to calculate the sensitivity of our photonic crystal to changes in the dielectric constant of the surrounding medium and evaluate its potential usefulness as a sensor. We find that while the frequency bandwidth for supercollimation in rods in significantly narrower than that for holes, rods are significantly more sensitive to perturbations; a sensor (such as a Mach–Zehnder interferometer) based on supercollimation in a slab of rods would only need to be about one-sixth of the length of a similar sensor based on slab of air holes. These results indicate that supercollimation in a rod slab would be better suited for sensing, while hole slabs would be more suitable for applications in communication.

6.3 Design of a supercollimating photonic crystal subject to fabrication constraints

Our first task was to design a photonic crystal that would support supercollimation at a free-space wavelength of 1550 μm, which was the optimal wavelength of operation for the infrared laser to be used in the experimental verification of supercollimation. The structure was to consist of a square lattice of 700 μm tall silicon rods (dielectric constant $\epsilon_{Si} = 12.4$) supported by a 3 μm thick substrate of SiO_2 ($\epsilon_{SiO_2} = 2.35$), and air elsewhere. Given these constraints, the main geometrical parameters left to

vary were the lattice spacing a and the diameter of the rods d. After calculating the equifrequency contours (using preconditioned conjugate-gradient minimization of the block Rayleigh quotient in a plane wave basis [41]) for a number of structures covering the parameter space for d and a, we eventually settled on a structure with $a = 437.5$ nm and $d = 250$ nm, whose equifrequency contours for the TM-like modes around the wavelength of interest are shown in Fig. 6-1(a).

6.4 Bandwidth analysis and comparison to a slab of air holes in silicon

Once the equifrequency contours are known, we can propagate a beam in the photonic crystal slab as follows: imagine that we form a focused monochromatic beam out of the Bloch modes lying on one of the contours in Fig. 6-1(a). On the plane defined by $x_{\|} = 0$ [$x_{\|}$ is the direction of propagation of the beam and is parallel to $k_{\|}$ indicated in Fig. 6-1(a)] each of these Bloch modes will have a relative phase dictated by the initial focusing of the beam, but after propagating up to the plane $x_{\|} = L$, each mode will have acquired an additional phase $e^{ik_{\|}L}$, where $k_{\|}$ is in principle different for each mode. (We ignore the additional phase $e^{-i\omega t}$ due to time evolution as it is the same for all modes in the beam and consequently does not contribute to diffraction.) The field profile at $x_{\|} = L$ is then found by resumming the phase-shifted modes at that position. In our computations, we approximate the modes on each contour as plane waves (identified by their wave-number $k_{\perp}$ perpendicular to the axis of propagation) and the initial beam as having the initial gaussian profile

$$E_z\left(x_{\perp}, x_{\|} = 0\right) = E_0 e^{-x_{\perp}^2/w_0^2}, \tag{6.1}$$

where E_0 is the magnitude of the electric field at the center of the beam and w_0 is the initial beam waist. The Fourier transform of the initial beam profile with respect to $x_{\perp}$ is then

$$\tilde{E}_z\left(k_{\perp}, x_{\|} = 0\right) = \frac{w_0 E_0}{\sqrt{2}} e^{-k_{\perp}^2 w_0^2/4}, \tag{6.2}$$

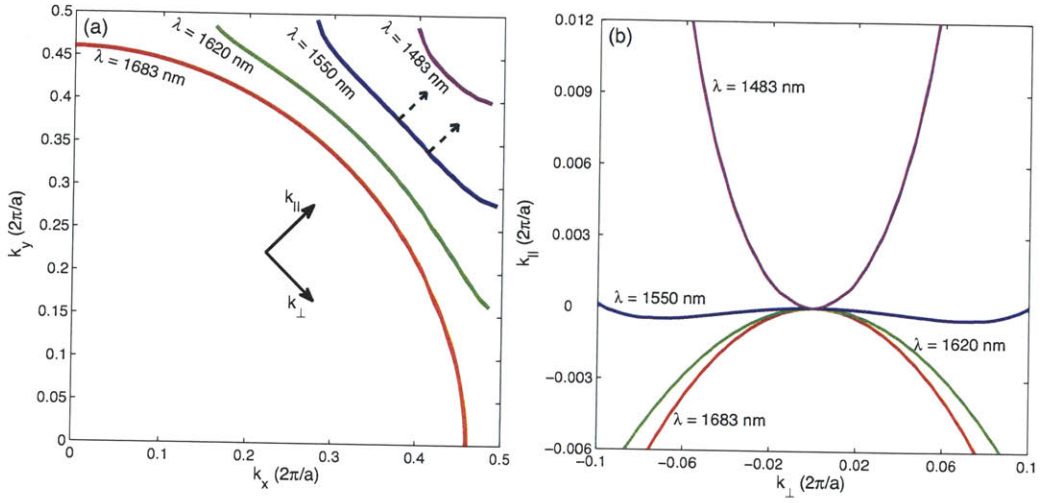

Figure 6-1: (a): Equifrequency contours of the first band (TM-like) of a rod slab in air. The lattice constant is $a = 437.5$ nm and each contour is labeled by its equivalent free space wavelength. The dimensions of the photonic crystal have been selected so as to achieve the flattest contour close to $\lambda = 1550$ nm (blue contour). The dashed arrows indicate the direction of the group velocity at the designated contour, while the solid arrows define the axes parallel ($k_{\|}$) and perpendicular ($k_{\perp}$) to the propagation of the beam. (b): Eigenfrequency contours plotted against the $k_{\perp}$–$k_{\|}$ axes after subtracting a constant from $k_{\|}$ so that all contours pass through the origin. These contours are then fitted to a fourth-order polynomial to extract the coefficients used in the beam-propagation method calculation.

and based on our earlier discussion, the field profile at $x_{\|} = L$ can be found by computing

$$E_z(x_{\perp}, L) = \frac{w_0 E_0}{2\sqrt{\pi}} \int_{-\infty}^{\infty} dk_{\perp} e^{ik_{\perp}x_{\perp} + ik_{\|}(k_{\perp})L - k_{\perp}^2 w_0^2/4}, \tag{6.3}$$

where $k_{\|}(k_{\perp})$ denotes the dependence of $k_{\|}$ on $k_{\perp}$, which we obtained by fitting a fourth-order polynomial to the equifrequency contours [Fig. 6-1(b)] of the photonic crystal.

As the beam propagates, its profile (Eq. 6.3) will deviate significantly from its initial gaussian shape. After experimenting with a few alternatives, we found that a robust definition of the spread of a beam was the width containing $\mathrm{erf}(\sqrt{2}) \simeq 0.9545$ of the beam intensity (which is $\propto |E_z|^2$). This definition has the desirable property of reducing to twice the beam waist when the beam propagation remains

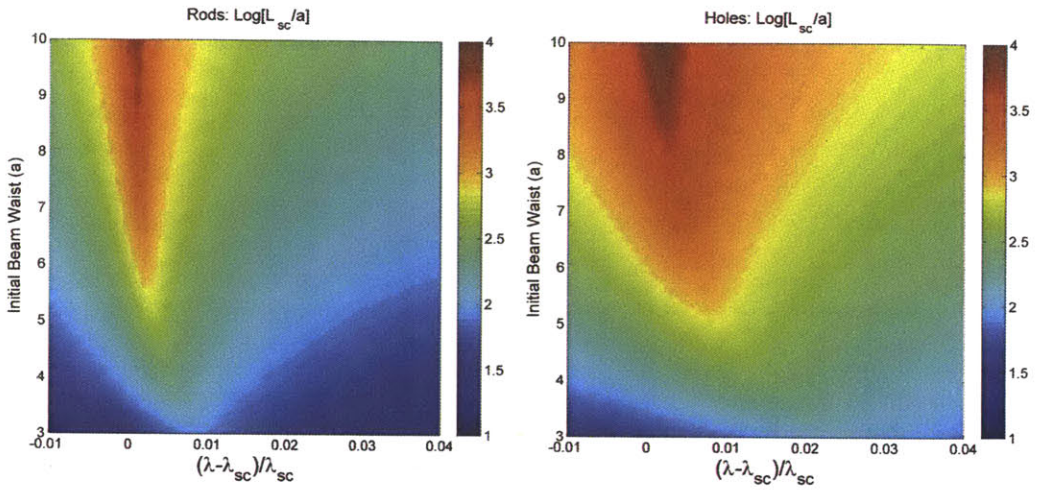

Figure 6-2: Bandwidth comparison between holes and rods showing the (base 10) logarithm of the supercollimation length L_{sc} as a function of the fractional detuning from the supercollimation wavelength λ_{sc} and the initial beam waist for a rod slab (left panel) and a hole slab (right panel).

gaussian (e.g., in free space) and also varies smoothly as a function of the propagation distance. (Another possible measure of the width of the beam, the full width at half maximum, did not fare well in that regard because the beam profile often became non-monotonic in our computations.) We then defined the supercollimation length L_{sc} as the distance at which the width of the beam would spread by a factor of $\sqrt{2}$ relative to its initial value. In the special case of free-space propagation, this definition conveniently reduces to the Rayleigh length ($L_R = \pi w_0^2/\lambda$) widely used in the theory of gaussian beams.

Once we had defined an appropriate figure of merit for the supercollimation, we used it to quantify the degree of supercollimation that can be achieved in a photonic crystal as the initial beam waist and wavelength of operation are varied. As a point of reference, we defined λ_{sc} as the wavelength at which the quadratic term in our fit of the equifrequency contours vanished ($\simeq$ 1545nm in our rod slab). For comparison, we performed an identical analysis for a hole slab structure (also made of silicon on a SiO_2 substrate, and with lattice spacing 350 nm, hole diameter 220 nm, and height 205 nm) in which supercollimation had been previously demonstrated [66]. One can see from

Fig. 6-2 that the hole structure has a considerably wider frequency bandwidth for supercollimation, which is due to its equifrequency contours being flatter and closer to the Γ point. Another striking property of Fig 6-2 is that the optimal wavelength for supercollimation varies as a function of the beam waist. This is because, for $\lambda > \lambda_{sc}$, the quadratic coefficient in the polynomial fit of the equifrequency contours becomes negative (Fig. 6-1) while the higher order term remains positive. This causes the contour to be effectively flatter for larger values of $k_{\perp}$. As the initial beam waist increases, the Fourier modes of the beam are more closely bunched about the origin (Eq. 6.2) meaning that the quadratic term dominates and the optimal wavelength asymptotes to λ_{sc}. Predictably, L_{sc} increases monotonically with the beam width since a wider beam experiences a flatter portion of the equifrequency contour.

6.5 Sensitivity analysis

We now turn to the analysis of how well our rod slab would be able to sense a perturbation in the dielectric properties of the surrounding medium. As a concrete picture of a sensor, we consider a Mach–Zehnder interferometer consisting of two arms of length L: one unperturbed and the other passing through a perturbed region with slightly different dielectric properties. As a collimated light beam propagates through the unperturbed arm, it acquires a phase $k \times L$, where k is the propagation constant. In order for the sensor to detect the perturbation, the perturbed light beam would have to acquire a large enough phase shift to interfere destructively with the unperturbed beam. Thus, if the propagation constant through the perturbed region is $k + \delta k$, the sensor can detect the perturbation if

$$\delta k \times L \simeq \pi. \tag{6.4}$$

We now need to relate δk to the perturbation in the dielectric properties of the medium surrounding the photonic crystal. Using first-order perturbation theory applied to Maxwell's equations [37], one finds that the fractional frequency shift of a given

Bloch mode due to a change $\delta\epsilon(\mathbf{r})$ in the dielectric profile is

$$\frac{\delta\omega}{\omega} = -\frac{1}{2}\frac{\int d\mathbf{r}\delta\epsilon(\mathbf{r})|\mathbf{E}(\mathbf{r})|^2}{\int d\mathbf{r}\epsilon(\mathbf{r})|\mathbf{E}(\mathbf{r})|^2}. \tag{6.5}$$

In case $\delta\epsilon$ is constant and limited to one domain, Eq. 6.5 reduces to

$$\frac{\delta\omega}{\omega} = -\sigma\left(\frac{\delta n}{n}\right), \tag{6.6}$$

where σ is the fraction of electric-field energy in the perturbed domain and $n = \sqrt{\epsilon_r}$ is the refractive index of the medium. δk is then readily found to be

$$\delta k = \sigma\left(\frac{\delta n}{n}\right)\left(\frac{\omega}{|\mathbf{v}_g|}\right). \tag{6.7}$$

For our rod slab at $\lambda_{sc} \simeq 1545$ nm, we find $\omega = 0.282 \times (2\pi c/a)$, $\sigma = 0.30$, and $|\mathbf{v}_g| = 0.223c$. Combining this with Eq. 6.4 we find that the length of a sensor capable of detecting a perturbation $\delta n/n$ needs to be

$$L_{\text{rod}} \simeq \left(\frac{n}{\delta n}\right) \times 0.58\ \mu\text{m}. \tag{6.8}$$

A 5 mm long sensor (of the order of the experimentally demonstrated supercollimation in a hole slab [66]) based on supercollimation in a rod slab should therefore be able to detect a relative shift in the refractive index as small as $\sim 10^{-4}$. A similar calculation for the hole slab results in

$$L_{\text{hole}} \simeq \left(\frac{n}{\delta n}\right) \times 3.4\ \mu\text{m}, \tag{6.9}$$

whence we see that the rod slab is approximately six times more sensitive than the hole slab. This is because the fraction of electric energy in air is roughly six times greater in the rod structure.

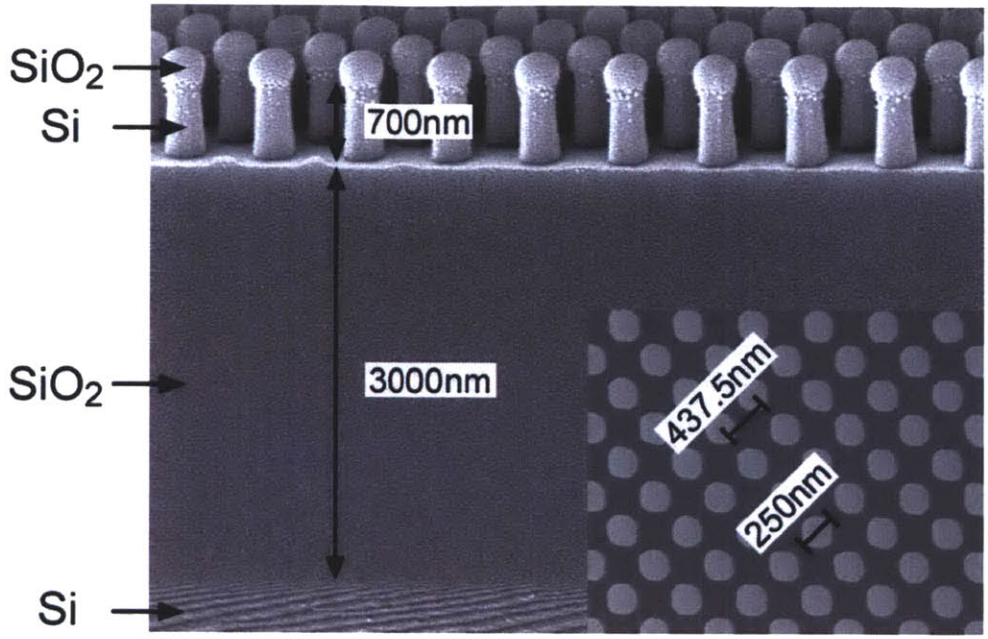

Figure 6-3: Side view SEM of the fabricated supercollimating photonic crystal. Inset: plan view SEM of the same crystal. (Image credit: Ta-Ming Shih.)

6.6 Experimental results

After we concluded our theoretical analysis, our collaborators fabricated a number of samples of the rod slab (Fig. 6-3) using a variety of photolithography and etching techniques [72]. They were then able to couple a tunable infrared laser source to the photonic crystal and, by detecting the light scattered out of the slab by imperfections in the structure (Fig. 6-4), were able to to observe supercollimation for up to 1000 lattice constants. The optimal wavelength for supercollimation varied between 1530 and 1550 nm depending on the sample and was therefore in good agreement with our numerical predictions.

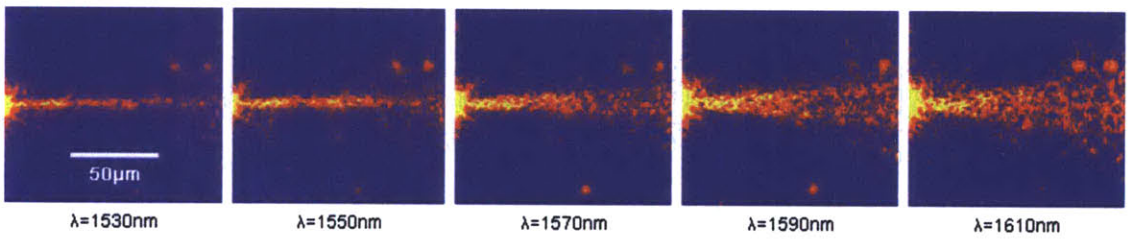

Figure 6-4: Plan view far-field infrared images showing the wavelength dependence of the propagating laser beam inside the photonic crystal of rods. The optimal wavelength for supercollimation for this particular sample is close to 1530 nm, and the beam diverges more strongly as the wavelength is detuned. The image is to scale, and its width is over 200 lattice periods wide. (Image credit: Marcus Dahlem.)

Chapter 7

Abrupt coupling between strongly dissimilar waveguides with 100% transmission

7.1 Summary

We present numerical experiments showing how coupled-mode theory can be systematically applied to join very dissimilar photonic crystal waveguides with 100% transmission. Our approach relies on appropriately tuning the coupling of the evanescent tail of a cavity mode to each waveguide. The transition region between the waveguides may be as short as a few lattice spacings. Moreover, this technique only requires varying a small number of parameters (one discrete and one continuous for each waveguide in our example) and the tuning to each waveguide may be done separately, greatly simplifying the computations involved.

7.2 Overview

In this chapter, we provide a general prescription for, and specific examples of, how abrupt interfaces between a photonic crystal cavity and two waveguides may be tailored so that 100% transmission between the waveguides is achieved. Photonic crys-

tals enable an extraordinary degree of control over the propagation of light and a wide variety of novel physical effects [83, 38, 37]. Connecting different photonic crystal devices in an efficient manner could be critical to enabling complex integrated photonic devices. Slow-light waveguides, for example, have greatly enhanced sensitivity to nonlinear effects, thus facilitating the design of compact electro-optical devices [82, 73, 4, 1], but coupling to them can be particularly challenging [63]. For a variety of applications, our proposal may present an alternative to approaches such as butt-coupling [54, 67], mode-field matching [53, 80], anti-reflection coating-like injectors [79, 15], optical stub tuners [8, 9], and tapered transitions between waveguides [52, 27, 40, 68, 69, 16, 62, 34, 56]. The approach explored here exploits the property known as "Q-matching" in the abstract framework of coupled-mode theory [29], which for photonic crystals as well as for our previously discussed resonant coils (Chaps. 3 and 4), provides a very accurate phenomenological approximation to the full physics, provided that the coupling coefficient between any two distinct structures is sufficiently weak. We begin by introducing three different photonic crystal waveguides within a square lattice of silicon rods in air. Next, we show how coupled-mode theory may be applied to split the overall problem into substantially more tractable parts by allowing each waveguide to be separately matched to a single-defect cavity. Finally, once all three waveguide-cavity structures are properly tuned, we check the validity of the tuning procedure and demonstrate 100% transmission by fully simulating the transmission for all combinations of two distinct waveguides. Both the tuning and verification are done via full simulations of Maxwell's equations with no approximation except for the discretization [60].

7.3 The three dissimilar waveguides

For concreteness, we consider three different kinds of waveguides formed by introducing linear defects into a two-dimensional square lattice (with lattice constant a) of rods of radius $r = a/4$ and permittivity $\epsilon_{\text{high}} = 12.25$ embedded in a dielectric material with $\epsilon_{\text{low}} = 2.25$. (These values of the dielectric constants approximately

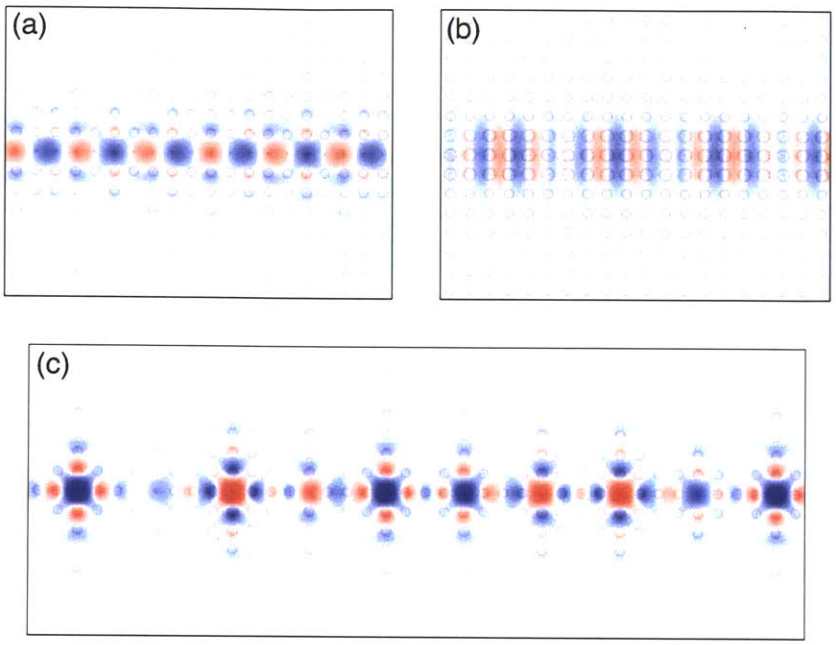

Figure 7-1: Images of the z-component (parallel to the rods) of the electric field of the TM modes at $\omega = 0.265 \times (2\pi c/a)$ of our three exemplar waveguides: a singly-wide linear defect waveguide (a), a triply-wide linear waveguide (b), and a coupled-cavity slow-light waveguide (CCW) with periodicity $4a$ (c). All three waveguides are single-mode (for TM modes) at the frequency indicated.

correspond to those for silicon and fused silica in the near infrared, respectively.) The first waveguide [Fig. 7-1(a)] is a standard linear defect waveguide formed by substituting one column of rods in the original square lattice by a column of rods with smaller radius $a/12$. The second waveguide [Fig. 7-1(b)] is a triply-wide linear defect wherein three adjacent columns of the square lattice are replaced with rods of larger radius $0.325a$, and the last waveguide [Fig. 7-1(c)] is a coupled-cavity waveguide [85, 59] (CCW) in which every fourth rod along a column is replaced with a rod of radius $a/12$. The permittivity of the defect rods is the same as that of the original rods (ϵ_{high}) in all three waveguides. Fig. 7-2 shows the dielectric function profiles for the three waveguides analyzed as well as the relevant TM bands (computed by preconditioned conjugate-gradient minimization of the block Rayleigh quotient in a plane wave basis [41]) and the projected band diagram for TM modes of the square

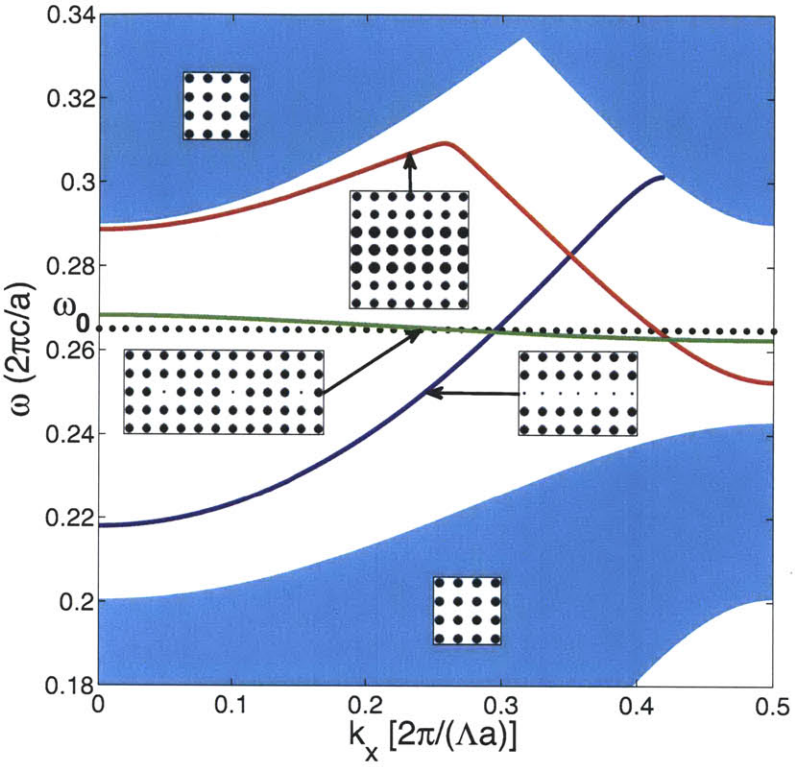

Figure 7-2: Projected band diagram along the Γ–X direction for TM modes in a square lattice of rods of radius $a/4$ (shaded region) and band structures for a singly-wide line defect, triply-wide line defect, and coupled-cavity waveguide (identified by their dielectric profile). The defect radii are, respectively, $a/12$, $0.325a$, and $a/12$. The constant Λ (x–axis of the figure) is 4 for the CCW and 1 for the other structures due to the longer primitive cell ($4a$) of the former along the direction of the propagation.

lattice of rods. Since the CCW has its inflection point (and thus zero group velocity dispersion) at the center-gap frequency $\omega_0 = 0.265 \times (2\pi c/a)$, we take ω_0 as the target frequency for which the transmission is to be maximized.

7.4 Design and tuning of the coupling cavity

We now turn to the design of a compact resonant cavity to mediate the transmission between any two waveguides. If we impose the requirement that the resonant structure be weakly coupled to each waveguide and that the direct coupling between

waveguides be in turn negligible compared to their interaction with the cavity, then the key phenomenon of interest is well described by the temporal coupled-mode theory equations introduced in Section 2.3:

$$\dot{A} = -i\omega_0 \left(1 - i\sum_m \frac{1}{2Q_m}\right) A + \sum_m \sqrt{\frac{\omega_0}{Q_m}} S_m^{(+)}, \tag{7.1}$$

$$S_m^{(-)} = -S_m^{(+)} + \sqrt{\frac{\omega_0}{Q_m}} A, \tag{7.2}$$

where $A(t)$ denotes the complex amplitude of the cavity's excitation and is normalized such that the energy associated with the cavity is $|A|^2$, ω_0 is the resonant frequency of the cavity, the index m denotes the different waveguides, and Q_m is the quality factor of the cavity's decay into waveguide m. $S_m^{(+)}$ and $S_m^{(-)}$ represent, respectively, the complex amplitudes of the waveguide modes going towards and away from the cavity, and are normalized such that the power flowing in each mode is given by $\left|S_m^{(\pm)}\right|^2$. A schematic of the coupled-mode theory of the particular system considered in this treatment (one cavity coupled to two waveguides) is shown in Fig. 2-1. The transmission $T(\omega) = \left|S_2^{(-)}/S_1^{(+)}\right|^2$ for this setup is readily found by solving Eqs. 7.1 and 7.2 when $S_1^{(+)}$ is set to a constant and $S_2^{(+)} = 0$:

$$T(\omega) = \frac{\omega_0^2/(Q_1 Q_2)}{(\omega_0 - \omega)^2 + \left(\frac{1}{2Q_1} + \frac{1}{2Q_2}\right)^2 \omega_0^2}, \tag{7.3}$$

which—as shown in Section 2.3—equals unity (100% transmission) at $\omega = \omega_0$ if $Q_1 = Q_2$, a property often referred to as the Q-matching condition [20]. It follows that we can approach the problem of coupling two dissimilar waveguides with a three-step process: 1) design a cavity that resonates at the desired frequency, 2) separately model the cavity in conjunction with a single waveguide and tune each cavity-waveguide interface so as to achieve a target coupling Q, and 3) as a check (if desired), simulate the full system with two waveguides and the cavity. For each step, we performed simulations using the finite-difference time-domain method [75] (FDTD), implemented in a freely available software package [60], with a resolution of

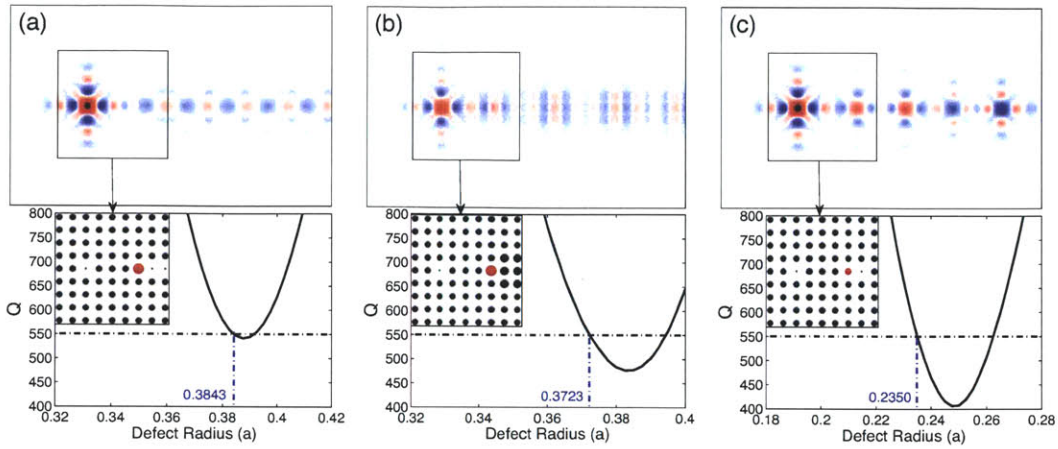

Figure 7-3: Results of a finite-difference time-domain (FDTD) simulation of a cavity resonant at $\omega_0 = 0.265 \times (2\pi c/a)$ decaying into a singly-wide line defect waveguide (a), a triply-wide line defect waveguide (b), and a slow-light coupled-cavity waveguide (c). The top panels show the z component (parallel to the rods) of the electric field. The insets show the dielectric profile of the area indicated. The lower panels show the dependence of the cavity Q on the defect radius of the rod closest to the waveguide (insets, in red). The latter are tuned so that the Q of the cavity is 550 in each case. The values of the defect radii indicated in blue are used in the full simulations of the coupled waveguides.

16 pixels per lattice spacing. In the first two steps, we used the filter-diagonalization method [51] to extract the resonant frequency and Q of the cavity and the waveguide. We found that a point-defect formed by replacing one lattice rod with a rod of same dielectric constant ϵ_{high} and radius $0.1095a$ had a resonant frequency within 0.05% of the target $\omega_0 = 0.265 \times (2\pi c/a)$. For tuning the Q of the cavity coupled to each waveguide (Fig. 7-3), we varied two parameters: the number of of lattice periods separating the cavity from the waveguide (a discrete parameter) and the radius of the rod closest to the waveguide. We found that at a separation of four lattice spacings, all three systems had local minima in the vicinity of $Q = 550$, which we chose as our target. (Note that it may often be desirable to tune Q to a value close to a local minimum, as this is where the slope of Q as a function of the continuous parameter is smallest, thereby improving the robustness of the tuning with respect to perturbations in the tuning parameter due to imperfections in the fabrication.)

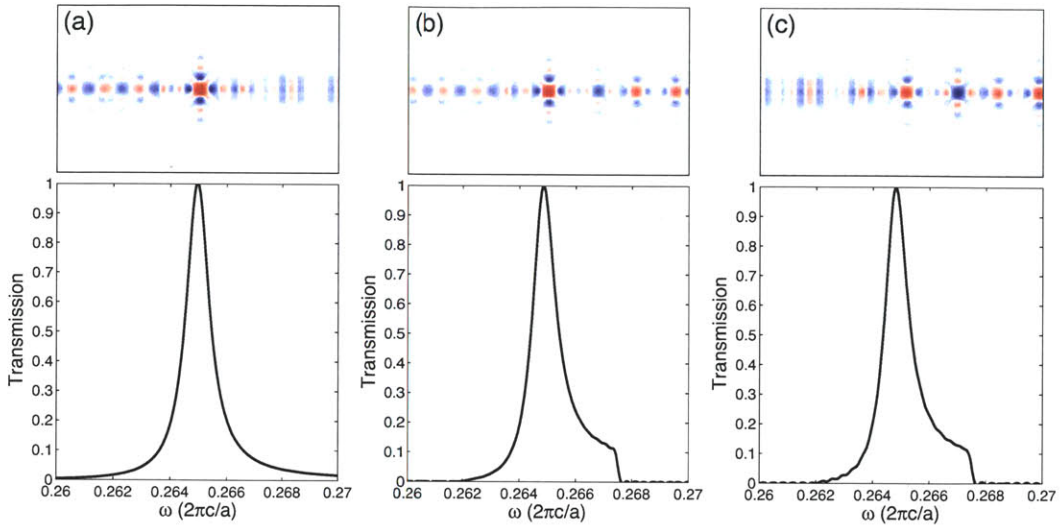

Figure 7-4: FDTD simulations showing the z component of the electric field (top panels) and the transmission spectrum of a singly-wide line defect waveguide coupling to triply-wide waveguide (a), a singly-wide waveguide coupling to a CCW (b), and a triply-wide waveguide coupling to a CCW (c). Each system is tuned to the points indicated (in blue) in Fig. 7-3 and exhibits 100% transmission near $\omega_0 = 0.265 \times (2\pi c/a)$.

7.5 Full simulation of the waveguide junctions

After finding the optimal tuning parameters for each system, we verified that all combinations of dissimilar waveguides coupled by means of the cavity and properly tuned intervening structure exhibited 100% transmission at $\omega = \omega_0$ by directly exciting the leftmost waveguide (Fig. 7-4) and measuring the flux through the second waveguide and the reflected flux in the first waveguide. We found the FDTD simulations of the direct transmission to be considerably more subtle than those for the tuning of the cavity Q, particularly in systems comprising a slow light waveguide. Although we terminated the waveguides with perfectly matched layers (PML [7, 47]) with the expectation that they would fully absorb the outgoing waves at the boundary of the computational cell, in practice we experienced significant reflection [61] that interfered with our calculation of the transmitted and reflected fluxes. As a work-around, we ensured that the computational cell was large enough (in the range of 1000–1500

lattice constants depending on the simulation) that any reflection from the boundary would not have time to propagate back to the locations through which the fluxes were computed before the end of the simulation. This had to be balanced with the requirement that the the simulation had to run for a sufficient time to allow the (unreflected) electromagnetic wave-packets to fully propagate through the flux locations (Fig. 7-5). Because of these subtleties and the necessity of modeling two waveguides simultaneously, these final simulations are considerably more numerically intensive than those shown in Fig. 7-3 and it would be far less practical to use them directly to search for the appropriate tuning parameters, especially for three-dimensional systems. Nevertheless, they fully bear out the predictions from the coupled-mode theory combined with a set of much simpler simulations.

7.6 Conclusion and outlook

Note that due to the symmetry of the square lattice of the underlying photonic crystal, the junctions shown in Fig. 7-3 could have just as well been used in a 90° bend coupling one waveguide to another. Indeed, the prescription outlined here may be applied directly to any system comprising two single-mode waveguides and a single-mode cavity that fulfills the condition of sufficiently weak coupling required for a coupled-mode theory treatment. It could, for instance, be used to couple modes of very different symmetry and polarization (e.g., TE to TM or TEM_{01} to HE_{11}) and is not limited to photonic crystals. Finally, it should be possible obtain broader transmission bandwidths by extending this technique to multi-mode cavities [74].

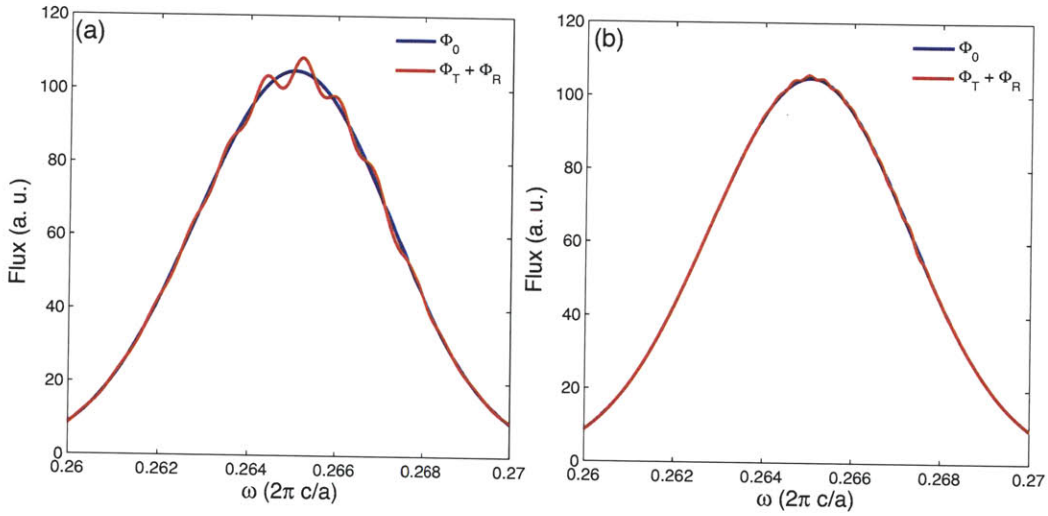

Figure 7-5: Example of a consistency check for the FDTD direct simulation of transmission from the singly-wide linear defect waveguide to the CCW [Fig. 7-4(b)]. Φ_0 denotes the spectrum of electromagnetic power that the source deposits in the linear defect waveguide. Φ_T is the flux spectrum measured through a plane in the CCW and Φ_R is the reflected flux spectrum measured through a plane in the linear defect waveguide. As there are no loss mechanisms, the condition $\Phi_0 = \Phi_T + \Phi_R$ should hold. If the simulation is run for only 2000 time units (c/a) after the source has been turned off, the electromagnetic fields have not finished propagating through the flux planes where Φ_R and Φ_T are measured, thus violating our consistency condition (a). If the fields propagate for 4000 time units after the the source is turned off, the equality is met to within $<$ 1% (b).

Chapter 8

Conclusion and possible directions for further research

Most of this thesis is devoted to topics related to wireless power transfer. Although we have demonstrated—theoretically and experimentally—the fundamental feasibility of efficient midrange power transfer through near-field electromagnetic interactions in the strongly coupled regime, analyzed potential efficiency improvements made possible by simultaneously powering multiple devices in the dilute regime, and proposed a novel design for an electrical conductor that could lead to significant improvements in the efficiency of the transfer and the miniaturization of the resonators, there are several outstanding problems whose treatment would lead to further gains in performance and, perhaps, a widespread adoption of this approach in practical applications. Within the realm of the coupled-mode theory formalism, it might be interesting to analyze a system that is in some ways the opposite of the dilute approximation we treated in Chapter 4: a daisy chain in which a source couples strongly to one device, which in turns couples strongly (and relays power) to another device (which is weakly coupled to the source), and so on. A particular case of this scenario was studied in [26], and it seems likely that systems of this kind could be exploited to substantially increase the distances over which wireless power transfer can be effected with good efficiency. Although it may be impractical to make general statements about arbitrary systems of multiple strongly coupled sources and devices, it is possi-

ble that a statistical approach to the general problem (e.g., by averaging over likely spatial configurations and applying a max-min condition on the overall efficiency or on the power delivered to each device) might lead to useful design guidelines for the resonators and their tuning parameters. We may also be able to obtain major performance gains by optimizing the physical design of the resonators; one possibility would be to perform a numerical optimization similar to that done in Chapter 5 for the electrical conductor design, but applied to the entire geometry of the resonators. The optimization could also be extended to cases where a resonator is embedded in a particular object and one has to account for the extraneous losses due to the object as well as the effect of the latter on the coupling of the resonator to other coils. Such an analysis would be of particular relevance to real-world applications of wireless power transfer.

We mentioned in Chapter 5 that one drawback of our electrical conductor consisting of concentric shells relative to litz wire is that, in order to enforce the optimal current distribution through the structure, each shell must be matched to a different impedance. While this can be done by brute force (e.g., by using a proper matching circuit), there may be simpler and more elegant solutions to this problem; perhaps a physical structure that couples to the shells and performs the impedance-matching in an economical way can be designed. It would also be useful to extend our analysis to cases consisting of multiple turns of concentric shell conductors (which may be approximated in 2D as parallel cylinders) and take into account the proximity losses induced by the overall magnetic field due to all the turns when performing the minimization of the resistance. Our treatment could also be extended to concentric structures with shapes other than cylindrical: since the Helmholtz equation is separable in elliptic cylindrical coordinates [55], the analytical solutions we found for cylindrical shells can be generalized to shells of confocal elliptic cylinders. Finally, it should be possible to fabricate our proposed conductor (and experimentally verify our predictions) using existing methods such as electroplating and electrodeposition and perhaps even by building on existing fiber-drawing techniques [6, 50, 18].

As noted at the end of Chapter 7, the Q-matching technique for coupling waveg-

uides could be applied to a much greater variety of modes than the particular examples we have considered, and is not limited to waveguides in photonic crystals (although in systems without a complete photonic band gap, the design of the coupling structure would need to take radiative losses into careful consideration). Since a major advantage of this approach is its relative computational simplicity, it may be particularly useful when applied to fully three-dimensional structures, and could therefore be of help in designing waveguide couplers for fabrication.

Bibliography

[1] S. P. Anderson, A. R. Shroff, and P. M. Fauchet. Slow light with photonic crystals for on-chip optical interconnects. *Adv. Opt. Tech.*, 2008:293531, 2008.

[2] T. Aoki, B. Dayan, E. Wilcut, W. P. Bowen, A. S. Parkins, T. J. Kippenberg, K. J. Vahala, and H. J. Kimble. Observation of strong coupling between one atom and a monolithic microresonator. *Nature*, 443:671, 2006.

[3] M. Augustin, R. Iliew, C. Etrich, D. Schelle, H.-J. Fuchs, U. Peschel, S. Nolte, E.-B. Kley, F. Lederer, and A. Tünnermann. Self-guiding of infrared and visible light in photonic crystal slabs. *Appl. Phys. B*, 81:313–319, 2005.

[4] T. Baba. Slow light in photonic crystals. *Nat. Photon.*, 2:465–473, 2008.

[5] J. P. Barton and D. R. Alexander. Fifth-order corrected electromagnetic field components for a fundamental gaussian beam. *J. Appl. Phys.*, 66:2800–2802, 1989.

[6] M. Bayindir, F. Sorin, A. F. Abouraddy, J. Viens, S. D. Hart, J. D. Joannopoulos, and Y. Fink. Metal-insulator-semiconductor optoelectronic fibres. *Nature*, 431:826, 2004.

[7] J.-P. Berenger. A perfectly matched layer for the absorption of electromagnetic waves. *J. Comput. Phys*, 114:185–200, 1994.

[8] S. Boscolo, C. Conti, M. Midrio, and C. G. Someda. Numerical analysis of propagation and impedance matching in 2-d photonic crystal waveguides with finite length. *J. Lightw. Tech.*, 20:304–310, 2002.

[9] S. Boscolo, M. Midrio, and T. F. Krauss. Y junctions in photonic crystal channel waveguides: high transmission and impedance matching. *Opt. Lett.*, 27:1001–1003, 2002.

[10] W. C. Brown. The history of power transmission by radio waves. *IEEE Trans. Microw. Th. Tech.*, 32:1230–1242, 1984.

[11] B. L. Cannon, J. F. Hoburg, D. D. Stancil, and S. C. Goldstein. Magnetic resonant coupling as a potential means for wireless power transfer to multiple small receivers. *IEEE Trans. Power Elec.*, 24:1819, 2009.

[12] S.-L. Chuang. A coupled mode formulation by reciprocity and a variational principle. *J. Lightw. Tech.*, LT-5:5–15, 1987.

[13] COMSOL Multiphysics, COMSOL Inc., www.comsol.com).

[14] L. W. Davis. Theory of electromagnetic beams. *Physical Review A*, 19:1177–1179, 1979.

[15] C. M. de Sterke, J. Walker, K. B. Dossou, and L. C. Botten. Efficient slow light coupling into photonic crystals. *Opt. Express*, 15:10984–10990, 2007.

[16] K. Dossou, L. C. Botten, C. M. de Sterke, R. C. McPhedran, A. A. Asatryan, S. Chen, and J. Brnovic. Efficient couplers for photonic crystal waveguides. *Opt. Comm.*, 265:207–219, 2006.

[17] W. A. Edson. *Vacuum-Tube Oscillators.* Wiley, New York, 1953.

[18] S. Egusa, Z. Wang, N. Chocat, Z. M. Ruff, A. M. Stolyarov, D. Shemuly, F. Sorin, P. T. Rakich, J. D. Joannopoulos, and Y. Fink. Multimaterial piezoelectric fibres. *Nature Materials*, 9:643, 2010.

[19] A. Esser and H.-C. Skudelny. A new approach to power supplies for robots. *IEEE Trans. Ind. Appl.*, 27:872, 1991.

[20] S. Fan, S. G. Johnson, J. D. Joannopoulos, C. Manolatou, and H. A. Haus. Waveguide branches in photonic crystals. *J. Opt. Soc. Am. B*, 18:162–165, 2001.

[21] S. Fan, W. Suh, and J. D. Joannopoulos. Temporal coupled-mode theory for the fano resonance in optical resonators. *J. Opt. Soc. Am. A*, 20:569–572, 2003.

[22] FCC 47 CFR Part 18, October 14, 2010.

[23] J. M. Fernandez and J. A. Borras. Contactless battery charger with wireless control link, U. S. Patent, 6,184,651 (2001).

[24] J. A. Ferreira. Improved analytical modeling of conductive losses in magnetic components. *IEEE Trans. Power Electron.*, 9:127–131, 1994.

[25] A. Grebennikov. *RF and Microwave Power Amplifier Design.* McGraw-Hill, New York, 2004.

[26] R. E. Hamam, A. Karalis, J. D. Joannopoulos, and M. Soljačić. Efficient weakly-radiative wireless energy transfer: An eit-like approach. *Ann. Phys.*, 324:1783, 2009.

[27] T. D. Happ, M. Kamp, and A. Forchel. Photonic crystal tapers for ultracompact mode conversion. *Opt. Lett.*, 26:1102–1104, 2001.

[28] A. Hardy and W. Streifer. Coupled mode theory of parallel waveguides. *J. Lightw. Tech.*, LT-3:1135–1146, 1985.

[29] H. A. Haus. *Waves and Fields in Optoelectronics.* Prentice-Hall, Englewood Cliffs, NJ, 1984.

[30] H. A. Haus and W. Huang. Coupled-mode theory. *Proceedings of the IEEE*, 79, 1991.

[31] H. A. Haus, W. P. Huang, S. Kawakami, and N. A. Whitaker. Coupled-mode theory of optical waveguides. *J. Lightw. Tech.*, LT-5:16–23, 1987.

[32] J. Hirai, T.-W. Kim, and A. Kawamura. Wireless transmission of power and information and information for cableless linear motor drive. *IEEE Trans. Power Electron.*, 15:21, 2000.

[33] W. P. Huang. Coupled-mode theory for optical waveguides: an overview. *J. Opt. Soc. Am. A*, 11:963–983, 1994.

[34] J. P. Hugonin, P. Lalanne, T. P. White, and T. F. Krauss. Coupling into slow-mode photonic crystal waveguides. *Opt. Lett.*, 32:2638–2640, 2007.

[35] IEEE Std C95.1-2005, IEEE Standard for Safety Levels with Respect to Human Exposure to Radio Frequency Electromagnetic Fields, 3 kHz to 300 GHz (IEEE, Piscataway, NJ, 2006).

[36] J. D. Jackson. *Classical Electrodynamics.* John Wiley and Sons, New York, 3rd edition, 1998.

[37] J. D. Joannopoulos, S. G. Johnson, J. N. Winn, and R. D. Meade. *Photonic Crystals: Molding the Flow of Light.* Princeton University Press, Princeton, second edition, 2008.

[38] S. John. Strong localization of photons in certain disordered dielectric superlattices. *Phys. Rev. Lett.*, 58:2486–2489, 1987.

[39] S. G. Johnson. The NLopt Nonlinear Optimization Package, http://ab-initio.mit.edu/nlopt.

[40] S. G. Johnson, P. Bienstman, M. A. Skorobogatiy, M. Ibanescu, E. Lidorikis, and J. D. Joannopoulos. Adiabatic theorem and continuous coupled-mode theory for efficient taper transitions in photonic crystals. *Phys. Rev. E*, 66:066608, 2002.

[41] S. G. Johnson and J. D. Joannopoulos. Block-iterative frequency-domain methods for maxwell's equations in a planewave basis. *Opt. Express*, 8(3):173–190, 2001.

[42] L. Ka-Lai, J. W. Hay, and P. G. W. Beart. Contact-less power transfer, U.S. patent 7,042,196.

[43] A. Karalis. *Novel photonic phenomena in nanostructured material systems with applications and Mid-range efficient insensitive Wireless Energy-Transfer.* ScD thesis, Massachusetts Institute of Technology, 2008.

[44] A. Karalis, J. D. Joannopoulos, and M. Soljačić. Efficient wireless non-radiative mid-range energy transfer. *Ann. Phys.*, 323:34, 2008.

[45] H. Kosaka, T. Kawashima, A. Tomita, M. Notomi, T. Tamamura, T. Sato, and S. Kawakami. Self-collimating phenomena in photonic crystals. *Appl. Phys. Lett.*, 74:1212, 1999.

[46] H. Kosaka, T. Kawashima, A. Tomita, T. Sato, and S. Kawakami. Photonic-crystal spot-size converter. *Appl. Phys. Lett.*, 74:268–270, 2000.

[47] M. Koshiba, Y. Tsuji, and S. Sasaki. High-performance absorbing boundary conditions for photonic crystal waveguide simulations. *IEEE Microwave Wirel. Compon. Lett*, 11:152–154, 2001.

[48] A. Kurs, A. Karalis, R. Moffatt, J. D. Joannopoulos, P. Fisher, and M. Soljačić. Wireless power transfer via strongly coupled magnetic resonances. *Science*, 317:83, 2007.

[49] L. D. Landau and E. M. Lifshitz. *Electrodynamics of Continuous Media, 2nd Edition.* Butterworth-Heinemann, Oxford, 1984.

[50] X. Lin, Y.-W. Shi, K.-R. Sui, X.-S. Zhu, K. Iwai, and M. Myagi. Fabrication and characterization of infrared hollow fiber with multi- sio2 and agi inner-coating layers. *Applied Optics*, 48:6765, 2009.

[51] V. A. Mandelshtam and H. S. Taylor. Harmonic inversion of time signals. *J. Chem. Phys.*, 107:6756–6769, 1997.

[52] A. Mekis and J. D. Joannopoulos. Tapered couplers for efficient interfacing between dielectric and photonic crystal waveguides. *J. Lightw. Tech.*, 19:861–865, 2001.

[53] E. Miyai and S. Noda. Structural dependence of coupling between a two-dimensional photonic crystal waveguide and a wire waveguide. *J. Opt. Soc. Am. B*, 21:67–72, 2004.

[54] N. Moll and G.-L. Bona. Comparison of three dimensional photonic crystal slab waveguides with two-dimensional photonic crystal waveguides: Efficient butt coupling in these photonic crystal waveguides. *J. Appl. Phys*, 93:4986–4991, 2003.

[55] P. M. Morse and H. Feshbach. *Methods of Theoretical Physics.* Feshbach Publishing, Minneapolis, 1981.

[56] A. Mutapcic, S. Boyd, A. Farjadpour, S. G. Johnson, and Y. Avniel. Robust design of slow-light tapers in periodic waveguides. *Eng. Optim.*, 41:365–384, 2009.

[57] X. Nan and C. R. Sullivan. An improved calculation of proximity-effect loss in high-frequency windings of round conductors. In *IEEE Power Electronics Specialists Conference*, pages 853–860, June 2003.

[58] New England Wire Litz Wire Catalog, http://www.newenglandwire.com.

[59] D. O'Brien, M. D. Settle, T. Karle, A. Michaeli, M. Salib, and T. F. Krauss. Coupled photonic crystal heterostructure nanocavities. *Opt. Express*, 15:1228–1233, 2007.

[60] A. F. Oskooi, D. Roundy, M. Ibanescu, P. Bermel, J. D. Joannopoulos, and S. G. Johnson. MEEP: A flexible free-software package for electromagnetic simulations by the FDTD method. *Comp. Phys. Comm.*, 181:687–702, January 2010.

[61] A. F. Oskooi, L. Zhang, Y. Avniel, and S. G. Johnson. The failure of perfectly matched layers and towards their redemption by adiabatic absorbers. *Optics Express*, 16:11376–11392, 2008.

[62] P. Pottier, M. Gnan, and R. M. De La Rue. Efficient coupling into slow-light photonic crystal channel guides using photonic crystal tapers. *Opt. Express*, 15:6569–6575, 2007.

[63] M. L. Povinelli, S. G. Johnson, and J. D. Joannopoulos. Slow-light, band-edge waveguides for tunable time delays. *Optics Express*, 13:7145–7159, 2005.

[64] M. J. D. Powell. Direct search algorithms for optimization calculations. *Acta Numerica*, 7:287, 1998.

[65] D. W. Prather, S. Shi, J. Murakowski, G. J. Scheider, A. Sharkawy, C. Chen, B. Miao, and R. Martin. Self-collimation in photonic crystal structures: a new paradigm for applications and device development. *J. Phys. D: Appl. Phys.*, 40:2635, 2007.

[66] P. T. Rakich, M. S. Dahlem, S. Tandon, M. Ibanescu, M. Soljačić, G. S. Petrich, J. D. Joannopoulos, L. A. Kolodziejski, and E. P. Ippen. Achieving centimetre-scale supercollimation in a large-area two-dimensional photonic crystal. *Nat. Mater.*, 5:93, 2006.

[67] P. Sanchis, P. Bienstman, B. Luyssaert, R. Baets, and J. Marti. Analysis of butt coupling in photonic crystals. *IEEE Jour. Quant. Electron.*, 40:541–550, 2004.

[68] P. Sanchis, J. Garcia, A. Martinez, F. Cuesta, A. Griol, and J. Marti. Analysis of adiabatic coupling between photonic crystal single-line-defect and coupled-resonator optical waveguides. *Opt. Lett.*, 28:1903–1905, 2003.

[69] P. Sanchis, J. Marti, W. Bogaerts, P. Dumon, D. Van Thourhout, and R. Baets. Experimental results on adiabatic coupling into soi photonic crystal coupled-cavity waveguides. *IEEE Photon. Tech. Lett.*, 17:1199, 2005.

[70] F. Segura-Quijano, J. García-Cantón, J. Sacristán, T. Osés, and A. Baldi. Wireless powering of single-chip systems with integrated coil and external wire-loop resonator. *Appl. Phys. Lett.*, 92:074102, 2008.

[71] S. Sensiper. *Electromagnetic wave propagation on helical conductors.* PhD thesis, Massachusetts Institute of Technology, 1951.

[72] T.-M. Shih, A. Kurs, M. Dahlem, G. Petrich, M. Soljavić, E. Ippen, L. Kolodziejski, K. Hall, and M. Kesler. Supercollimation in photonic crystals composed of silicon rods. *Appl. Phys. Lett.*, 93:131111, 2008.

[73] M. Soljačić, S. G. Johnson, S. Fan, M. Ibanescu, E. Ippen, and J. D. Joannopoulos. Photonic-crystal slow-light enhancement of nonlinear phase sensitivity. *J. Opt. Soc. Am. B*, 19:2052, 2002.

[74] W. Suh, Z. Wang, and S. Fan. Temporal coupled-mode theory and the presence of non-orthogonal modes in lossless multimode cavities. *IEEE Jour. Quantum Electron.*, 40:1511–1518, 2004.

[75] A. Taflove and S. C. Hagness. *Computational Electrodynamics: The Finite Difference Time Domain Method.* Artech, Norwood, MA, 2000.

[76] F. E. Terman. *Radio Engineer's Handbook.* McGraw-Hill, New York, 1943.

[77] N. Tesla. Apparatus for Transmitting Electrical Energy, U.S. patent 1,119,732, (1914).

[78] T. A. Vanderelli, J. G. Shearer, and J. R. Shearer. Method and apparatus for a wireless power supply, U.S. patent 7,027,311.

[79] P. Velha, J. P. Hugonin, and P. Lalanne. Compact and efficient injection of light into band-edge slow-modes. *Opt. Express*, 15:6102–6112, 2007.

[80] Y. A. Vlasov and S. J. McNab. Coupling into the slow light mode in slab-type photonic crystal waveguides. *Opt. Lett.*, 31:50–52, 2006.

[81] L. Wu, M. Mazilu, and T. F. Krauss. Beam steering in planar-photonic crystals: from superprism to supercollimator. *Jour. Lightw. Tech.*, 21:561, 2003.

[82] Y. Xu, R. K. Lee, and A. Yariv. Propagation and second-harmonic generation of electromagnetic waves in a coupled-resonator optical waveguide. *J. Opt. Soc. Am. B*, 17:387–400, 2000.

[83] E. Yablonovitch. Inhibited spontaneous emission in solid-state physics and electronics. *Phys. Rev. Lett.*, 58:2059–2026, 1987.

[84] T. Yamashita and C. Summers. Evaluation of self-collimated beams in photonic crystals for optical interconnect. *IEEE Journal on Selected Areas in Communications*, 23:1341–1347, 2005.

[85] A. Yariv, Y. Xu, R. K. Lee, and A. Scherer. Coupled-resonator optical waveguide: a proposal and analysis. *Opt. Lett.*, 24:711–713, 1999.